Monthly Notices
of the
ROYAL ASTRONOMICAL SOCIETY

MNRAS **483,** 5459–5479 (2019)
Advance Access publication 2018 December 17

doi:10.1093/mnras/sty3396

Type II supernovae as distance indicators at near-IR wavelengths

Ó. Rodríguez ,[1,2]★ G. Pignata,[1,2] M. Hamuy,[2,3] A. Clocchiatti,[2,4] M. M. Phillips,[5] K. Krisciunas,[6] N. I. Morrell,[5] G. Folatelli,[7,8] M. Roth,[5,9] S. Castellón,[5] I. S. Jang,[10] Y. Apostolovski,[1,2] P. López,[3] S. Marchi,[3] R. Ramírez[3] and P. Sánchez[3,11]

[1]*Departamento de Ciencias Fisicas, Universidad Andres Bello, Avda. Republica 252, Santiago, Chile*
[2]*Millennium Institute of Astrophysics, Casilla 36-D Santiago, Chile*
[3]*Departamento de Astronomía, Universidad de Chile, Casilla 36-D Santiago, Chile*
[4]*Instituto de Astrofísica, Pontificia Universidad Católica de Chile, Casilla 306 Santiago 22, Chile*
[5]*Carnegie Observatories, Las Campanas Observatory, Casilla 60 La Serena, Chile*
[6]*Department of Physics and Astronomy, Texas A&M University, College Station, TX 77843, USA*
[7]*Facultad de Ciencias Astronómicas y Geofísicas, UNLP, IALP, CONICET, Paseo del Bosque S/N, B1900FWA La Plata, Argentina*
[8]*Kavli Institute for the Physics and Mathematics of the Universe (WPI), The University of Tokyo, 5-1-5 Kashiwanoha, Kashiwa, Chiba 277-8583, Japan*
[9]*GMTO Corporation, Avenida Presidente Riesco 5335, Suite 501, Las Condes, Santiago, Chile*
[10]*Leibniz-Institut für Astrophysik Potsdam, D-14482 Potsdam, Germany*
[11]*European Southern Observatory, Casilla 19001 Santiago 19, Chile*

Accepted 2018 December 12. Received 2018 December 7; in original form 2018 June 22

ABSTRACT

Motivated by the advantages of observing at near-IR wavelengths, we investigate Type II supernovae (SNe II) as distance indicators at those wavelengths through the Photospheric Magnitude Method (PMM). For the analysis, we use *BVIJH* photometry and optical spectroscopy of 24 SNe II during the photospheric phase. To correct photometry for extinction and redshift effects, we compute total-to-selective broad-band extinction ratios and *K*-corrections up to $z = 0.032$. To estimate host galaxy colour excesses, we use the colour–colour curve method with the *V*–*I* versus *B*–*V* as colour combination. We calibrate the PMM using four SNe II in galaxies having Tip of the Red Giant Branch distances. Among our 24 SNe II, nine are at $cz > 2000\,\mathrm{km\,s^{-1}}$, which we use to construct Hubble diagrams (HDs). To further explore the PMM distance precision, we include into HDs the four SNe used for calibration and other two in galaxies with Cepheid and SN Ia distances. With a set of 15 SNe II we obtain an HD rms of 0.13 mag for the *J*-band, which compares to the rms of 0.15–0.26 mag for optical bands. This reflects the benefits of measuring PMM distances with near-IR instead of optical photometry. With the evidence we have, we can set the PMM distance precision with *J*-band below 10 per cent with a confidence level of 99 per cent.

Key words: supernovae: general – galaxies: distances and redshifts – distance scale.

1 INTRODUCTION

Type II supernovae (SNe II) are the explosive end of massive stars ($M_{\mathrm{ZAMS}} > 8\,\mathrm{M}_{\odot}$) that retain an important amount of hydrogen in their envelopes at the moment of the explosion. These events, consequence of the gravitational collapse of their iron cores, are characterized by a luminosity comparable to the total luminosity of their host galaxies, which make them interesting objects for distance measurements.

The pioneering work of Kirshner & Kwan (1974) marks the beginning of the use of SNe II as distance indicators. In their work they applied the Expanding Photosphere Method (EPM, a variant of the Baade–Wesselink method) to two SNe II, using optical photometry and spectroscopy during the photospheric phase (the phase between the maximum light and the transition to the radioactive tail) to estimate angular and physical sizes, respectively. For the first implementation of the EPM, Kirshner & Kwan (1974) assumed SNe II emit like blackbodies. Years after, Wagoner (1981) demonstrated that the flux of SNe II is diluted as a consequence of their scattering-dominated atmospheres, making necessary SN II atmosphere models to quantify that effect and thus to correct derived distances. Since then, the EPM has been applied using different theoretical atmosphere models (e.g. Eastman, Schmidt & Kirshner 1996; Dessart & Hillier 2005) to an ample number of SNe II (e.g. Schmidt, Kirshner & Eastman 1992; Schmidt et al. 1994; Hamuy

★ E-mail: olrodrig@gmail.com

2001; Dessart et al. 2008; Jones et al. 2009; Bose & Kumar 2014; Gall et al. 2016, 2018), where the typical EPM distance precision is found to be about 15 per cent.

Empirically, Hamuy & Pinto (2002) found a correlation between the bolometric luminosity at 50 d since explosion and the expansion velocity of the photosphere at the same epoch. This is due to the fact that a more energetic explosion corresponds to a more luminous SN with higher envelope expansion velocities. The latter correlation is the basis of the Standardized Candle Method (SCM), which allows to estimate distances using photometry and expansion velocities inter- or extrapolated at 50 d since explosion. The SCM has been applied to several SN II sets (e.g. Nugent et al. 2006; Poznanski et al. 2009; Olivares E. et al. 2010; D'Andrea et al. 2010; de Jaeger et al. 2015, 2017b; Gall et al. 2018), yielding a distance precision of about 12–14 per cent.

Despite the apparent differences between the EPM and the SCM, Kasen & Woosley (2009) showed that the SCM is a recasting of the EPM at 50 d since explosion. Additionally, by means of SN II models, they proposed a generalization of the SCM, which can be applied in any epoch during the photospheric phase. The same idea was investigated empirically by Rodríguez et al. (2014, hereafter R14), who called it the Photospheric Magnitude Method (PMM) to the SCM generalization. Measuring distances with all expansion velocities available during the photospheric phase decreases observational errors and reduces uncertainties introduced by the interpolation/extrapolation at a certain fiducial epoch. The PMM distance precision is around 6–11 per cent (R14).

For the EPM, SCM, and PMM, optical spectroscopy is necessary in order to estimate expansion velocities. Since the spectroscopy is more time consuming than photometry, expansion velocities are not always available. For this reason, de Jaeger et al. (2015) proposed a method based solely on photometry to standardize SNe II, known as the Photometric Colour Method (PCM). de Jaeger et al. (2017b) applied the PCM to an SN II sample with redshift up to 0.5, finding that the PCM distance precision is around 17 per cent.

Most of the distance measurements with the latter methods have been performed with optical photometry. However, observing at near-IR wavelengths has two clear benefits that, in principle, can improve their use as distance indicators:

(1) *Near-IR light is less affected by dust*. Methods to measure colour excess due to SNe II host galaxies (e.g. Schmidt et al. 1992; Krisciunas et al. 2009; Olivares E. et al. 2010; Poznanski, Prochaska & Bloom 2012; R14; Pejcha & Prieto 2015) are still not well established. Therefore, it is propitious to observe at near-IR wavelengths in order to reduce the effect of miscalculation of the colour excess. Moreover, the estimation of a representative extinction curve along the SN II line of sight is still controversial. Assuming the family of extinction curves of Cardelli, Clayton & Mathis (1989), some studies are in favour of a Galactic $R_V = 3.1$ (e.g. Pejcha & Prieto 2015), while other authors found results in favour of lower values (Poznanski et al. 2009; Olivares E. et al. 2010; de Jaeger et al. 2015). Since the choice of a certain extinction curve has more impact at optical than at near-IR wavelengths (e.g. Schlafly et al. 2016), it is preferable to perform photometric observations at those wavelengths in order to diminish systematics induced by the assumption of an incorrect extinction curve.

(2) *Contamination by metal lines is less severe at near-IR wavelengths*. Among the few metal lines identified in the near-IR, we remind: in the *J*-band range there is a feature at $\lambda = 1.2$ μm possibly due to an Si I multiplet (Valenti et al. 2015), Mg I λ1.53 μm is detected in the *H*-band range (Maguire et al. 2010b; Valenti et al. 2015; Yuan et al. 2016), while in the *K*-band range the Brackett γ is possibly blended with Na I (Dall'Ora et al. 2014). The low number and weakness of metal lines reduce the risk of systematic effects produced by differences in progenitor metallicity (e.g. Dessart et al. 2014; Anderson et al. 2016).

Schmidt et al. (1992) had already pointed out the benefits of measuring distances to SNe II using near-IR photometry. However, at present, there have been very few systematic studies (e.g. Schmidt et al. 1992, Hamuy et al. 2001 for the EPM; Maguire et al. 2010a, de Jaeger et al. 2015 for the SCM). In particular, Maguire et al. (2010a) suggested that it may be possible to reduce the scatter in the Hubble Diagram (HD) to 0.1–0.15 mag (distance precision of 5–7 per cent) using near-IR instead of optical photometry. However, this result is based on the analysis of a set of 12 SNe II, 11 of them at $z < 0.01$, so being highly affected by peculiar velocities. To test this promising result, de Jaeger et al. (2015) applied the SCM to a set of 24 SNe II at $0.01 < z < 0.04$, obtaining an HD rms of 0.28 mag (distance precision of 13 per cent) for the *J*-band and therefore questioning the improvements of the SCM distance precision using near-IR photometry.

The goal of this study is to investigate the PMM distance precision using near-IR photometry.

We organize our work as follows. In Section 2 we describe the photometric and spectroscopic data. In Section 3 we present the PMM developed in R14. In Section 4 we develop an algorithm to achieve non-parametric light-curve fitting. In Sections 5 and 6 we compute Galactic total-to-selective broad-band extinction ratios and *K*-corrections for *BVIJHK* bands, respectively. In Section 7 we compute host galaxy total-to-selective broad-band extinction ratios and host galaxy colour excesses through the analysis of colour–colour curves. In Section 8 we estimate expansion velocities and explosion epochs. In Section 9 we apply the PMM to our SN II sample, constructing HDs for *BVIJH* bands. Discussion about the PMM distance precision and systematics are in Section 10. In Section 11 we present our conclusions.

2 OBSERVATIONAL MATERIAL

We base our work on data obtained over the course of the Carnegie Type II Supernova Survey (CATS; PI: Hamuy, 2002–2003), a program whose main objective was to study nearby ($z < 0.05$) SNe II. Optical photometry and spectroscopy, along with some near-IR photometry, were obtained with the 1-m Swope, 2.5-m du Pont, and 6.5-m Magellan Baade and Clay telescopes at Las Campanas Observatory. A few additional optical images were obtained with the 0.9-m and 1.5-m telescopes at Cerro Tololo Inter-American Observatory. During the CATS survey, 34 SNe II were observed. Optical photometry and spectroscopy of these SNe II, along with the description of the data reduction, is presented in Galbany et al. (2016) and Gutiérrez et al. (2017), respectively. Next, we briefly summarize the general techniques used to obtain the near-IR photometric data, which will be released in a forthcoming publication.

2.1 Near-IR photometric data

The near-IR photometric observations were obtained with the *JHK* bands mounted in the Swope Telescope IR camera and the Wide Field IR Camera on the du Pont Telescope. Images where processed with a collection of IRAF[1] tasks. These include dark subtraction,

[1] IRAF is distributed by the National Optical Astronomy Observatory, which is operated by the Association of Universities for Research in Astronomy

flat-field correction, sky subtraction, image registration, and stacking. Instrumental magnitudes were obtained using the point spread function (PSF) technique, implemented in the SNOOPY[2] package. The near-IR magnitudes of the reference stars were calibrated using standard star fields obtained soon before or after the target field with an airmass similar to the target field.

2.2 Sample of supernovae

Among the 34 SNe II observed over the course of the CATS survey, we select a subset of 10 SNe II which comply with the following requirements: (1) having at least two photometric measurements in the *BVIJH* bands at 35–75 d since explosion (see Section 9), and (2) having at least one measurement of the expansion velocity at an epoch covered by the photometry mentioned in point 1. To this sample, we add 14 SNe II from the literature. Table 1 lists our final sample of 24 SNe II, which includes the SN name (Column 1), the name of the host galaxy, and its type (Columns 2 and 3), the heliocentric SN redshift and its source (Columns 4 and 5), host galaxy distance measured with Cepheids, the Tip of the Red Giant Branch (TRGB), or SN Ia (Column 6), Galactic colour excess (Column 7), and references for the data (Column 8). We also use optical and near-IR spectra of SNe II with the purpose of computing total-to-selective broad-band extinction ratios (Sections 5 and 7) and *K*-corrections (Section 6), and to estimate explosion epochs (Section 8.2).

3 PHOTOSPHERIC MAGNITUDE METHOD

The absolute magnitude of an SN II during the photospheric phase depends strongly on the temperature and the size of the photosphere (e.g. Kasen & Woosley 2009; R14; Pejcha & Prieto 2015). The latter can be estimated from the velocity of the material instantaneously at the photosphere (hereafter, photospheric velocity, $v_{\rm ph}$) and the time since the SN explosion epoch t_0, under the assumption of homologous expansion (e.g. Kirshner & Kwan 1974). R14 found that the time since explosion works better than the *V–I* colour (used as a proxy for temperature) to standardize the brightness of SNe II (see Fig. 9 in R14), showing that for a given band x the absolute magnitude in any moment t_i during the photospheric phase, $M_{x,\Delta t_i,v_{{\rm ph},i}}$, can be parametrized as

$$M_{x,\Delta t_i,v_{{\rm ph},i}} = a_{x,\Delta t_i} - 5\log\left(\frac{v_{{\rm ph},i}}{5000\ {\rm km\ s^{-1}}}\right). \quad (1)$$

Here, $\Delta t_i \equiv (t_i - t_0)/(1+z)$ is the elapsed time since the explosion in the SN rest frame at redshift z, and $a_{x,\Delta t_i}$ is a function that can be calibrated empirically. Previously, Kasen & Woosley (2009) found similar results for the SN II brightness standardization, but using SN II models.

With the knowledge of t_0 and a measurement of $v_{\rm ph}$ in any stage of the photospheric phase, we can compute the absolute magnitude at t_i (equation 1) and, therefore, compute the SN distance modulus given by

$$\mu_{x,i} = m^{\rm corr}_{x,i} - a_{x,\Delta t_i} + 5\log\left(\frac{v_{{\rm ph},i}}{5000\ {\rm km\ s^{-1}}}\right), \quad (2)$$

(AURA) under cooperative agreement with the National Science Foundation.

[2]SNOOPY is a package for SN photometry using PSF fitting and/or template subtraction developed by E. Cappellaro. A package description can be found at http://sngroup.oapd.inaf.it/snoopy.html

$$m^{\rm corr}_{x,i} = m_{x,i} - A^{\rm G}_{x,i} - K_{x,i} - A^{\rm h}_{x,i}. \quad (3)$$

Here, $m_{x,i}$ is the apparent magnitude, $A^{\rm G}_{x,i}$ and $A^{\rm h}_{x,i}$ are the Galactic and host galaxy broad-band extinction, respectively, and $K_{x,i}$ is the *K*-correction. If more than one measurement of $v_{\rm ph}$ is available, then we compute the distance modulus through a likelihood maximization (see Section 9.1).

4 LIGHT-CURVE FITS

In equation (2) we need all quantities at the same epoch. Being more time consuming, spectroscopy is, in general, less abundant than photometry, so performing photometric interpolations is a reasonable choice. Previous efforts to fit SN II light curves use both parametric and non-parametric methods. Parametric methods assume parametric functions that capture the behaviour of the light curve from early to late stages, where parameters are obtained through least-square minimization (e.g. Olivares E. et al. 2010) or through Bayesian methodologies (e.g. Sanders et al. 2015). Non-parametric methods are based on non-parametric regressions (NPR) like local regressions (e.g. Olivares 2008) and Gaussian processes (e.g. de Jaeger et al. 2017a). Since the light curves of the SNe in our sample are, in general, well sampled, we prefer to use NPR methods for the light-curve fitting, thus avoiding the use of heuristic models.

In this work we make use of LOESS, an NPR method that performs polynomial fits over local intervals along the domain (Cleveland, Grosse & Shyu 1992). To perform a LOESS fit, we have to specify: (1) the class of the local polynomial, which can be linear or quadratic, (2) the smoothing parameter, which defines the neighbourhood size around each element of the independent variable, where data can be well approximated by the aforementioned local polynomial, and (3) the distribution of random errors, which can be normal or symmetric (for more details, see Cleveland et al. 1992). We assume the null hypothesis that residuals are normally distributed, which can be checked with a normality test. An optimal value for the smoothing parameter can be obtained from data using the 'an' information criterion (AIC, Akaike 1974, see Appendix A). Therefore, to perform a LOESS fit, we only have to decide the local polynomial. We choose a quadratic polynomial in order to give more freedom to the LOESS fitting procedure. When the LOESS routine cannot perform a fit (e.g. for light curves with less than six points), we perform a low-order (linear or quadratic) polynomial fit.

To test whether photometry errors can account for the observed dispersion around the light-curve fit, $f^{\rm fit}_{x,t}$ (in flux units), we compute its log-likelihood given by

$$\ln\mathcal{L} = -0.5\sum_i\left(\ln(\sigma^2_{f_{x,i}} + \sigma^2_{x,{\rm int}}) + \frac{(f_{x,i} - f^{\rm fit}_{x,t_i})^2}{\sigma^2_{f_{x,i}} + \sigma^2_{x,{\rm int}}}\right), \quad (4)$$

where $f_{x,i}$ and $\sigma_{f_{x,i}}$ are the apparent magnitude and its error in flux units, respectively, and $\sigma_{x,{\rm int}}$ is the intrinsic error. If an intrinsic error is necessary to maximize the log-likelihood, then we add it in quadrature to the photometry errors and perform again the light-curve fitting. We repeat this process until an intrinsic error is not necessary.

To test the normality of the residuals, we use the Rescaled Moment (RM; Imon 2003) test (see Appendix A). Among all light-curve fits, 80 per cent have residuals with RM p-values ≥ 0.05, for which the hypothesis that residual are normally distributed cannot be rejected within a confidence level (CL) of 95 per cent. For the remaining 20 per cent, light-curve fits are still unbiased and consistent, but the confidence interval (CI) of the parameters may be

Table 1. SN II sample.

SN	Host galaxy	Host type†	$cz_{\rm helio}$ (km s^{-1})	Source‡	$\mu^{\star}_{\rm host}$ (mag)	$E_{\rm G}(B–V)^{\diamond}$ (mag)	References*
1999em	NGC 1637	SAB(rs)c	800 ± 50	L02	30.21 ± 0.15$^{\oslash,\triangleleft}$	0.035 ± 0.006	a, b, c, d, e
2002gd	NGC 7537	SAbc?	2536 ± 59	here	–	0.058 ± 0.009	a, f, g, h
2002gw	NGC 922	SB(s)cd	3143 ± 31	here	–	0.016 ± 0.003	a, f
2002hj	NPM1G +04.0097	–	7079 ± 20	here	–	0.101 ± 0.016	a, f
2003B	NGC 1097	SB(s)b	1141 ± 52	here	–	0.023 ± 0.004	a, f
2003E	MCG –4–12–4	Sc?	4484 ± 21	here	–	0.041 ± 0.007	a, f
2003T	UGC 4864	SA(r)ab	8368 ± 6	NED	–	0.027 ± 0.004	a, f
2003bl	NGC 5374	SB(r)bc?	4295 ± 41	here	–	0.023 ± 0.004	a, f
2003bn	LEDA 831618	–	3897 ± 25	here	–	0.056 ± 0.009	a, f
2003ci	UGC 6212	Sb	9052 ± 21	here	–	0.051 ± 0.008	a, f
2003cn	IC 849	SAB(rs)cd	5430 ± 162	NED	–	0.018 ± 0.003	a, f
2003hn	NGC 1448	SAcd?	1305 ± 35	S05	31.25 ± 0.07$^{\otimes}$	0.012 ± 0.002	a, d, f, i
2004et	NGC 6946	SAB(rs)cd	40 ± 2	NED	29.39 ± 0.14$^{\otimes}$	0.293 ± 0.047	h, j, k, l, m, n
2005ay	NGC 3938	SA(s)c	850 ± 26	here	–	0.018 ± 0.003	h, o
2005cs	M51a	SA(s)bc	463 ± 3	NED	29.66 ± 0.06$^{\otimes}$	0.032 ± 0.005	h, p, q, r
2008in	M61	SAB(rs)bc	1566 ± 2	NED	–	0.019 ± 0.003	f, o, s
2009N	NGC 4487	SAB(rs)cd	905 ± 21	here	–	0.018 ± 0.003	t
2009ib	NGC 1559	SB(s)cd	1304 ± 162	NED	31.72 ± 0.20$^{\triangle}$	0.026 ± 0.004	u, v
2009md	NGC 3389	SA(s)c	1308 ± 162	NED	–	0.023 ± 0.004	w
2012A	NGC 3239	IB(s)m	753 ± 162	NED	–	0.027 ± 0.004	x
2012aw	M95	SB(r)b	778 ± 4	NED	29.89 ± 0.07$^{\otimes}$	0.024 ± 0.004	y, z, aa
2012ec	NGC 1084	SA(s)c	1407 ± 162	NED	–	0.023 ± 0.004	bb
2013ej	M74	SA(s)c	657 ± 1	NED	29.95 ± 0.06$^{\otimes}$	0.060 ± 0.010	r, cc, dd, ee
2014G	NGC 3448	I0	1160 ± 84	here	–	0.010 ± 0.002	ff

Notes: †From NASA/IPAC Extragalactic Database (NED).
‡Source of the heliocentric SN redshift. L02: Leonard et al. (2002); S05: Sollerman et al. (2005); here: this work.
⋆Host galaxy distance moduli measured with Cepheids (⊘), TRGB (⊗) with the Jang & Lee (2017b) calibration, or with SN Ia (△).
$^{\diamond}$Galactic colour excesses from Schlafly & Finkbeiner (2011), with an error of 16 per cent (Schlegel, Finkbeiner & Davis 1998).
$^{\triangleleft}$Saha et al. (2006) distance was shifted by −0.19 ± 0.13 mag to be consistent with the Riess et al. (2016) calibration (Section 9.1).
∗(a) Galbany et al. (2016); (b) Hamuy et al. (2001); (c) L02 (d) Krisciunas et al. (2009); (e) Saha et al. (2006); (f) Gutiérrez et al. (2017); (g) Spiro et al. (2014); (h) Faran et al. (2014a); (i) Hatt et al. (2018); (j) Sahu et al. (2006); (k) Maguire et al. (2010b); (l) Tikhonov (2014); (m) Murphy et al. (2018); (n) Anand, Rizzi & Tully (2018); (o) Hicken et al. (2017); (p) Pastorello et al. (2006); (q) Pastorello et al. (2009); (r) McQuinn et al. (2017); (s) Roy et al. (2011); (t) Takáts et al. (2014); (u) Takáts et al. (2015); (v) Brown et al. (2010); (w) Fraser et al. (2011); (x) Tomasella et al. (2013); (y) Bose et al. (2013); (z) Dall'Ora et al. (2014); (aa) Rizzi et al. (2007); (bb) Barbarino et al. (2015); (cc) Yuan et al. (2016); (dd) Dhungana et al. (2016); (ee) Bose et al. (2015); and (ff) Terreran et al. (2016).

untrustworthy (Doane & Seward 2016). Anyway, in this work, to prevent any shortcoming related to the non-normality of the residuals, we perform simulations to compute CIs.

To compute the CI around a light-curve fit, we perform 10^4 simulations varying randomly the photometry according to its error. For each realization we perform a LOESS (or a low-order polynomial) fit, thus obtaining 10^4 simulated light curves per band. These simulations will allow us to compute its probability density function (pdf) at different epochs.

Fig. 1 shows results of the aforementioned fitting procedure applied to the SN II light curves used in this work, where solid lines are the LOESS (or low-order polynomial) fits, while shaded regions indicate values between the 10th and the 90th percentile, i.e. the 80 per cent CI.

5 GALACTIC BROAD-BAND EXTINCTION

In equation (3), the Galactic broad-band extinction in a photometric band x is given by

$$A^{\rm G}_{x,i} \equiv -2.5 \log \left(\frac{\int d\lambda_{\rm o} S_{x,\lambda_{\rm o}} F_{\lambda_{\rm r},i} \lambda_{\rm r} 10^{-0.4(A^{\rm h}_{\lambda_{\rm r}} + A^{\rm G}_{\lambda_{\rm o}})}}{\int d\lambda S_{x,\lambda_{\rm o}} F_{\lambda_{\rm r},i} \lambda_{\rm r} 10^{-0.4 A^{\rm h}_{\lambda_{\rm r}}}} \right) \quad (5)$$

(Olivares 2008). Here, $\lambda_{\rm o}$ is the wavelength in the observer's frame, $\lambda_{\rm r} = \lambda_{\rm o}/(1+z)$ is the wavelength in the SN rest frame at redshift z, $S_{x,\lambda_{\rm o}}$ is the x-band transmission function, $F_{\lambda_{\rm r},i}$ is the spectral energy distribution (SED) of the SN at epoch t_i. $A^{\rm G}_{\lambda_{\rm o}}$ and $A^{\rm h}_{\lambda_{\rm r}}$ are the Galactic and host galaxy monochromatic extinctions, respectively, given by

$$A^{\rm G}_{\lambda_{\rm o}} = R^{\rm G}_{\lambda_{\rm o}} \cdot E_{\rm G}(B-V), \quad (6)$$

$$A^{\rm h}_{\lambda_{\rm r}} = R^{\rm h}_{\lambda_{\rm r}} \cdot E_{\rm h}(B-V), \quad (7)$$

where $R_\lambda \equiv A_\lambda/E(B–V)$ is the extinction curve for our Galaxy ($R^{\rm G}_\lambda$) and hosts ($R^{\rm h}_\lambda$), and $E_{\rm G}(B–V)$ and $E_{\rm h}(B–V)$ are the Galactic and host galaxy colour excess, respectively.

Since the SED of SNe II evolve with time, we expect that the broad-band extinction $A^{\rm G}_{x,i}$ also evolve with time.[3] As the SED of SNe II has a blackbody nature, hereafter we use the intrinsic $B–V$ colour (a proxy for temperature) to represent its evolution.

In a previous work, Olivares (2008) computed the dependence of $A^{\rm G}_V$ on $B–V$. In this work, in order to convert Galactic colour excesses

[3]We remark the difference between a monochromatic extinction A_λ, which is constant for a fixed wavelength λ, and a broad-band extinction $A_{x,i}$, which depends on the SED and the x-band transmission function.

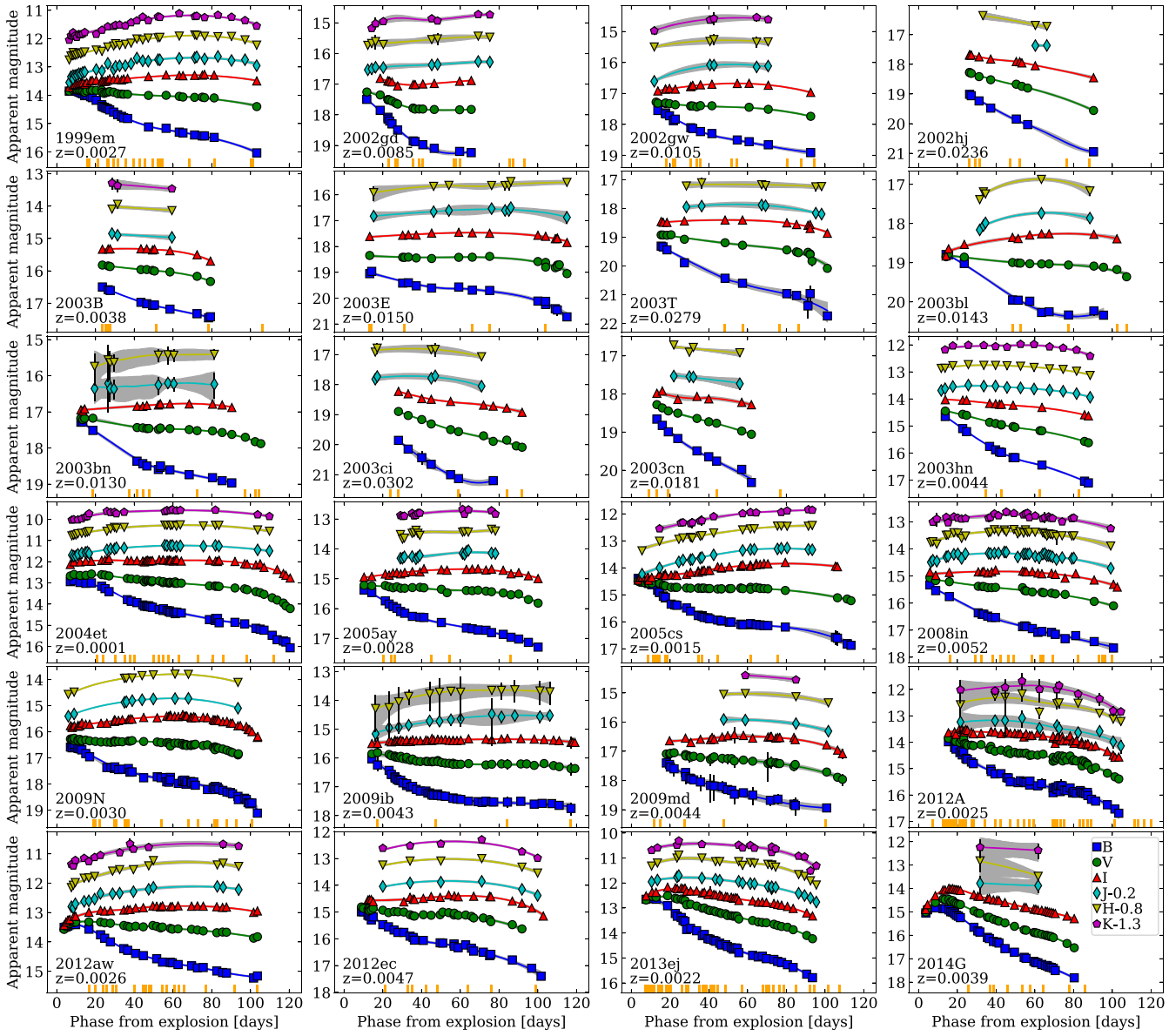

Figure 1. Light curves of SNe II used in this work. The estimated explosion epoch of each SN is used as reference time. Orange ticks mark the epochs of the spectroscopy. Solid lines and shaded regions correspond to the light-curve fits and its 80 per cent CIs, respectively.

directly into Galactic broad-band extinctions suitable for SNe II, we compute the Galactic total-to-selective broad-band extinction ratios $R^{\rm G}_{x,i}$, such that

$$A^{\rm G}_{x,i} \equiv R^{\rm G}_{x,i} \cdot E_{\rm G}(B-V). \quad (8)$$

With the purpose of obtaining representative $R^{\rm G}_{x,i}$ values for a local SN II sample through equations (8) and (5), we use: (1) a library of dereddened and deredshifted SN II spectra (see Appendix B), (2) colour excesses and redshifts from the following representative ranges: $E_{\rm G}(B–V) = 0.0–0.36$ mag, $E_{\rm h}(B–V) = 0.0–0.83$ mag, which were taken from the SN sample reported in R14, and $z = 0.0–0.032$, and (3) an extinction curve to redden the spectra for both our Galaxy and hosts. For the latter, since a representative extinction curve along the line of sight of SNe II is still controversial, we adopt the Fitzpatrick (1999) extinction curve with $R_V = 3.1$. For each spectrum, we perform 10^4 simulations picking randomly values of $E_{\rm G}(B–V)$, $E_{\rm h}(B–V)$, and z from the aforementioned ranges, adopting the median as the $R^{\rm G}_{x,i}$ representative value and the 80 per cent CI as its error.

The left-hand side of Fig. 2 shows the $R^{\rm G}_{x,i}$ values as a function of $B–V$ for BVI bands. There is a clear dependence of $R^{\rm G}_{B,i}$ and $R^{\rm G}_{V,i}$ on $B–V$. The y-axis scale at the left-hand side of Fig. 2 is the same in the three panels, so we can see that the redder the band the less the dependence on $B–V$, with $R^{\rm G}_{I,i}$ being nearly constant. This behaviour is due to the blackbody nature of the SN II SED, where for the longer wavelengths there is a less dependence of the SED slope on temperature.

To express the dependence of $R^{\rm G}_{x,i}$ on $B–V$ we perform polynomial fits. The latter, unlike NPR methods like LOESS, allow to perform corrections in an easy and less time-consuming way (see Appendix C).

To determine the optimal degree for the polynomial fit, we consider two criteria: the AIC and the Bayesian information criterion (BIC, Schwarz 1978). For more details, see Appendix A. Based

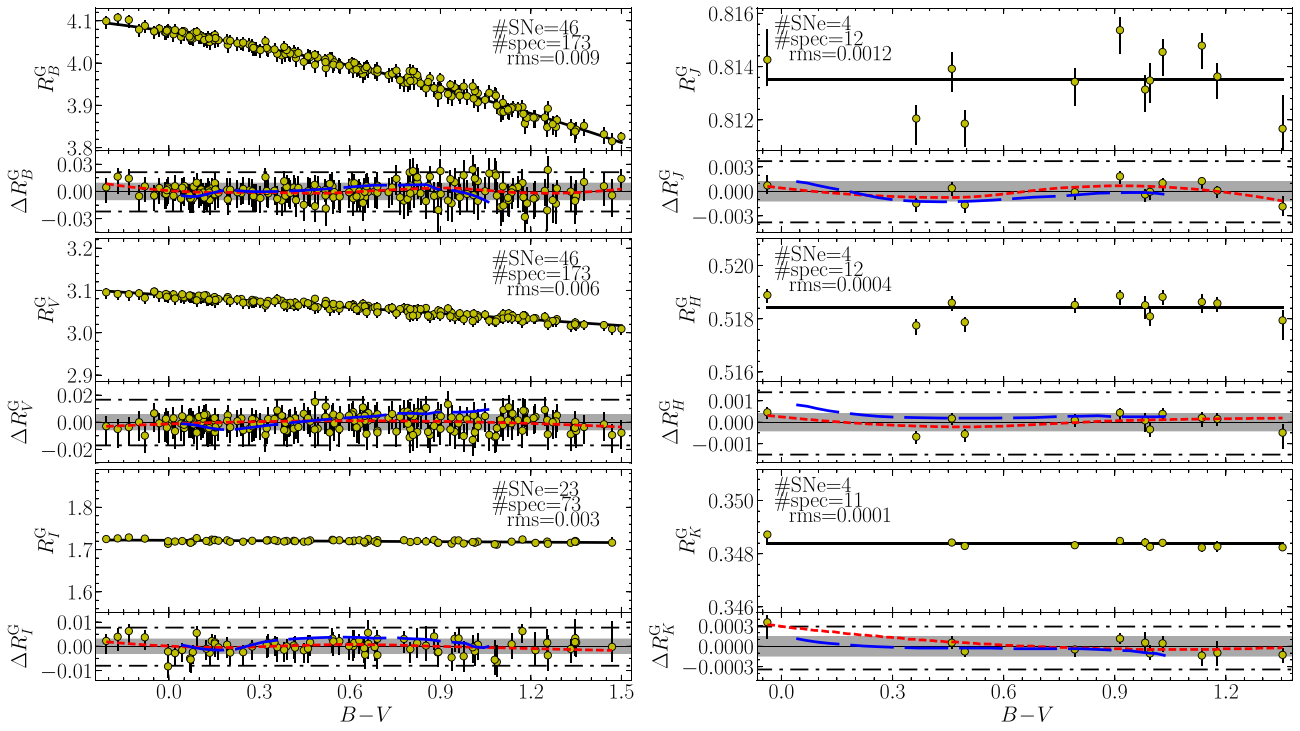

Figure 2. Galactic total-to-selective broad-band extinction ratios for *BVI* (left-hand panel) and *JHK* (right-hand panel) for SNe II as a function of the intrinsic *B–V* colour, along with residuals. Solid black lines correspond to the polynomial fits, red short-dashed lines correspond to LOESS regressions to the residuals, while blue long-dashed lines correspond to residuals between the m15mlt3 model (Dessart et al. 2013) and polynomial fits from observations. Grey regions indicate values within one rms, while black dash-dotted lines are the inner fences.

on evidence ratios (Table F1), for the *B*-, *V*-, and *I*-band, the AIC favours degrees ≥ 3, ≥ 1, and ≥ 1, respectively, while the BIC favours degrees between 2 and 6, 1 and 3, and 1 and 4, respectively. Results for both criteria are consistent. By the principle of parsimony (a.k.a. Occam's razor), we adopt the lowest degrees, i.e. 2, 1, and 1 for the *B*-, *V*-, and *I*-band, respectively. For *JHK* bands (right-hand side of Fig. 2) we adopt constant values. Although the small number of near-IR spectra means that the results are not fully statistically robust, we are confident about the negligible dependence of $R^{\rm G}_{x,i}$ on *B–V* for *JHK* bands based on the small rms values we obtained ($\lesssim$0.001).

Once the optimal polynomial degrees for $R^{\rm G}_x$ versus *B–V* are determined, we perform 10^4 bootstrap resampling of the data in order to compute the polynomial fit parameters and their errors, adopting the median as the representative value. Results are summarized in Table F2.

The bottom of each panel in Fig. 2 shows the residuals of the polynomial fit. To identify possible outliers we use the Tukey (1977) rule, where values below Q1 − 1.5(Q3 − Q1) or above Q3 + 1.5(Q3 − Q1) (known as inner fences, where Q1 and Q3 are the first and third quartile, respectively) are considered outliers. The few points detected as outliers are consistent with being within inner fences considering their errors, so we do not discard them from the analysis. To analyse possible trends not captured by the polynomial fit, we perform a LOESS regression (red short-dashed line) to the residuals. Variations in the LOESS fits are mostly within one rms, meaning that the evolution of $R^{\rm G}_x$ on *B–V* can be well represented by a polynomial fit of degree determined with the AIC/BIC. For all bands we obtain RM *p*-values >0.05, which means that we cannot reject the null hypothesis that residual are normally distributed (95 per cent CL). Based on this, we can treat the $R^{\rm G}_x$ rms error as a normal one.

For comparison, we compute $R^{\rm G}_x$ for *BVIJHK* bands using synthetic spectra of the m15mlt3 model of Dessart et al. (2013). Residuals between the m15mlt3 model and polynomial fits from observations (blue long-dashed lines in Fig. 2) are mostly contained within one rms.

6 *K*-CORRECTION

The *K*-correction in a photometric band x is given by

$$K_{x,i} \equiv -2.5\log(1+z) + K^s_{x,i}, \tag{9}$$

$$K^{\rm s}_{x,i} = 2.5\log\left(\frac{\int d\lambda_{\rm o} S_{x,\lambda_{\rm o}} F_{\lambda_{\rm o},i}\lambda 10^{-0.4A^{\rm h}_{\lambda_{\rm o}}}}{\int d\lambda_{\rm r} S_{x,\lambda_{\rm o}} F_{\lambda_{\rm r},i}\lambda_{\rm r} 10^{-0.4A^{\rm h}_{\lambda_{\rm r}}}}\right) \tag{10}$$

(Olivares 2008), being $K^{\rm s}_{x,i}$ the selective term. We proceed in the same way than in Section 5, but now the evolving SED is modified by SN host galaxy colour excess and redshift.

As in Section 5 we aim for an analytical expression for $K^{\rm s}_x$, for which we perform polynomial surface fits as a function of *B–V* and z. Since $K_x = 0$ for $z = 0$, any z-independent term on the $K^{\rm s}_x$ polynomial fit is zero. Dividing by z, the polynomial surface to adjust will be of the form

$$K^{\rm s}_x/z = \sum_{j_1=0}^{\mathcal{O}_{B-V}} \sum_{j_2=0}^{\mathcal{O}_{z,j_1}} a_{j_1,j_2} z^{j_2} (B-V)^{j_1}, \tag{11}$$

being $\mathcal{O}_{B-V}$ and $\mathcal{O}_{z,j_1}$ the orders in *B–V* and z, respectively, and a_{j_1,j_2} the fit parameters.

To determine the orders $\mathcal{O}_{B-V}$ and $\mathcal{O}_{z,i}$, we generate 10^5 spectral samples, where for each sample we assign to each spectrum a ran-

dom redshift up to 0.032. For each realization, we obtain optimal order values using the AIC/BIC and the principle of parsimony. In all cases we obtain that K_x^s/z depends only on B–V, i.e. it is z-independent for $z \leq 0.032$.

Fig. 3 shows the K_x^s/z values as a function of B–V for *BVI* (left-hand side) and *JHK* (right-hand side). We perform the same analysis than in Section 5. For *BVI* bands we adopt straight lines, while for *JHK* bands we fit constant values (see Table F1). Results are summarized in Table F2. Variations of the LOESS fits to the residuals are within one rms, meaning that the dependence of K_x^s/z on B–V can be well represented by the polynomial fit of degree determined with the AIC/BIC. For all bands we obtain RM p-values >0.05, which means that we cannot reject the null hypothesis that residual are normally distributed (95 per cent CL). Based on the latter, we can treat the K_x^s/z rms error as a normal one.

7 HOST GALAXY BROAD-BAND EXTINCTION

In equation (3), the host galaxy broad-band extinction in a photometric band x is given by

$$A^{\rm h}_{x,i} \equiv -2.5 \log \left(\frac{\int d\lambda S_{x,\lambda_{\rm o}} F_{\lambda_{\rm o},t} \lambda_{\rm o} 10^{-0.4 A^{\rm h}_{\lambda_{\rm o}}}}{\int d\lambda_{\rm o} S_{x,\lambda_{\rm o}} F_{\lambda_{\rm o},t} \lambda_{\rm o}} \right) \quad (12)$$

(Olivares 2008). We proceed in the same way than in Sections 5 and 6, but now the evolving SED is modified only by the SN host galaxy colour excess.

Similar to Section 5, we define the host galaxy total-to-selective broad-band extinction ratios $R^{\rm h}_{x,i}$, such that

$$A^{\rm h}_{x,i} \equiv R^{\rm h}_{x,i} \cdot E_{\rm h}(B-V). \quad (13)$$

The optimum $R^{\rm h}_x$ versus B–V polynomials and their parameters are summarized in Table F2.

R14 showed that for SNe II the B–V versus V–I colour–colour curve (C3) can be used to estimate $E_{\rm h}(B–V)$ through the method proposed by Natali et al. (1994), which was originally developed to estimate interstellar colour excess for open clusters.

The C3 method states that, under the assumptions that (1) the C3 can be well-represented by a straight line, and (2) all SNe II have the same C3 (which means the same slope and intercept), the host galaxy colour excess can be estimated with the formula

$$E_{\rm h,i}(B-V) = \frac{1}{R^{\rm h}_{c_x,i}} \frac{n_{S,i} - n_{S,{\rm zp}}}{\gamma_{S,i} - {\rm M}\{m_S\}} \quad (14)$$

(e.g. Munari & Carraro 1996; R14). Here, $S \equiv \{c_x, c_y\}$ indicates the colours used as x- and y-axis in the colour–colour diagram, corrected for Galactic colour excess and K-correction. ${\rm M}\{m_S\}$ is the median of a set of SN II C3 slopes $\{m_S\}$, $n_{S,i} = c_{y,i} - {\rm M}\{m_S\} \times c_{x,i}$ and $n_{S,{\rm zp}}$ are the y-intercept of the C3 linear fit using a fixed slope ${\rm M}\{m_S\}$ and that of the SN II less affected by colour excess, respectively. $R^{\rm h}_{c,i} = R^{\rm h}_{x_1,i} - R^{\rm h}_{x_2,i}$ for a colour $c = x_1 - x_2$, and $\gamma_{S,i} = R^{\rm h}_{c_y,i}/R^{\rm h}_{c_x,i}$ is the slope of the reddening vector. The subindex i in equation (14) denotes the dependence of $R^{\rm h}_{x,i}$ on the intrinsic B–V, so equation (14) must be evaluated separately at each point of the C3. In principle, one colour–colour observation is enough to estimate the colour excess; however, more observations allow to check internal consistency and reduce observational errors.

The C3 method relies strongly on the aforementioned two assumptions. In a previous work, R14 assumed the linearity of C3s based on the blackbody nature of the SED of SNe II during the photospheric phase, while assumption 2 was adopted based on the dependence of the emergent flux mainly on temperature displayed by SN II atmosphere models (e.g. Eastman et al. 1996; Jones et al. 2009). In this work we show that C3s can indeed be expressed as straight lines for several colour combinations (see Appendix C). Therefore, the major source of systematics comes from assumption 2. There are indeed some effects, like the line blanketing, that modify the SED continuum shape. In addition, differences in photometric systems (S-correction; Stritzinger et al. 2002) are expected to produce further changes on C3 parameters. Therefore, it is propitious to search for a colour combination where the effect of a colour excess on a C3 is greater than the effect of systematics.

An analysis of the effect of systematics on the C3 y-intercept is beyond the scope of this work because it requires an ample set of unreddened SNe II. However, the effect of systematics on C3 slopes and its consequent effects on the $E_{\rm h}(B–V)$ estimation through the C3 method can be quantified in a simple way.

The presence of dust along the line of sight produces a vertical displacement of the C3 (for a graphical representation, see R14) where, following equation (14), the magnitude of the displacement and its rms error are

$$\left| n_{S,i} - n_{S,{\rm zp}} \right| = E_{\rm h}(B-V) \cdot R^{\rm h}_{c_x,i} \cdot \left| \gamma_{S,i} - {\rm M}\{m_S\} \right|, \quad (15)$$

$${\rm rms}(\left| n_{S,i} - n_{S,{\rm zp}} \right|) \approx E_{\rm h}(B-V) \cdot R^{\rm h}_{c_x,i} \cdot {\rm rms}\{m_S\}, \quad (16)$$

respectively. In equation (16), we do not include the error induced by errors in $\gamma_{S,i}$, which is lower that 17 per cent of the uncertainty induced by the error in ${\rm M}\{m_S\}$. In order to find the colour combination that maximizes the dust effect (equation 15) and minimizes its error (equation 16), we define the quantity (a signal-to-noise ratio)

$$\xi_{S,i} \equiv \frac{\left| n_{S,i} - n_{S,{\rm zp}} \right|}{{\rm rms}(\left| n_{S,i} - n_{S,{\rm zp}} \right|)} \approx \frac{\left| \gamma_{S,i} - {\rm M}\{m_S\} \right|}{{\rm rms}\{m_S\}}. \quad (17)$$

Therefore, the most appropriate colour set S to compute $E_{\rm h}(B–V)$ with the C3 method is one that maximizes $\xi_{S,i}$.

Fig. 4 shows the $\xi_{S,t}$ values for all possible independent colour combinations with the *BVIJH* bands, using the ${\rm M}\{m_S\}$ and ${\rm rms}\{m_S\}$ values computed with our SN II sample (see Appendix C), and using $B–V = 0.0$ and 1.4, which are typical colours at the start and end of the photospheric phase, respectively. We do not include the K-band in this analysis because of the scarcity of SNe II with photometry in that band. The best colours combinations, independent of the intrinsic B–V, are those involving B–V, with V–I versus B–V the best. For this combination we obtain ${\rm M}\{m_S\} = 0.45 \pm 0.07$. We remark that colour combinations that do not include the B-band have $\xi_{S,t} \lesssim 1.0$, which indicates that the noise induced by intrinsic differences of C3 slopes is greater than the effect of host galaxy dust, and therefore those combinations are not suitable for $E_{\rm h}(B–V)$ measurement through the C3 method. We point out that colour combinations under the diagonal correspond to those above the diagonal but with the axes exchange. In principle they give the same information. However, by construction, they maximize displacement in x-axis instead of y-axis.

To compute the pdf of $n_{S,{\rm zp}}$ for $S = \{B–V, V–I\}$, we use the data of SN 2003bn and SN 2013ej, which are affected by a negligible host galaxy colour excess (R14), maximizing the likelihood of a straight line with slope 0.45 ± 0.07. With this process, we obtain a pdf with median of 0.107 mag and rms = 0.053 mag. Since the RM p-value for the latter distribution is >0.05, we treat it as a normal distribution.

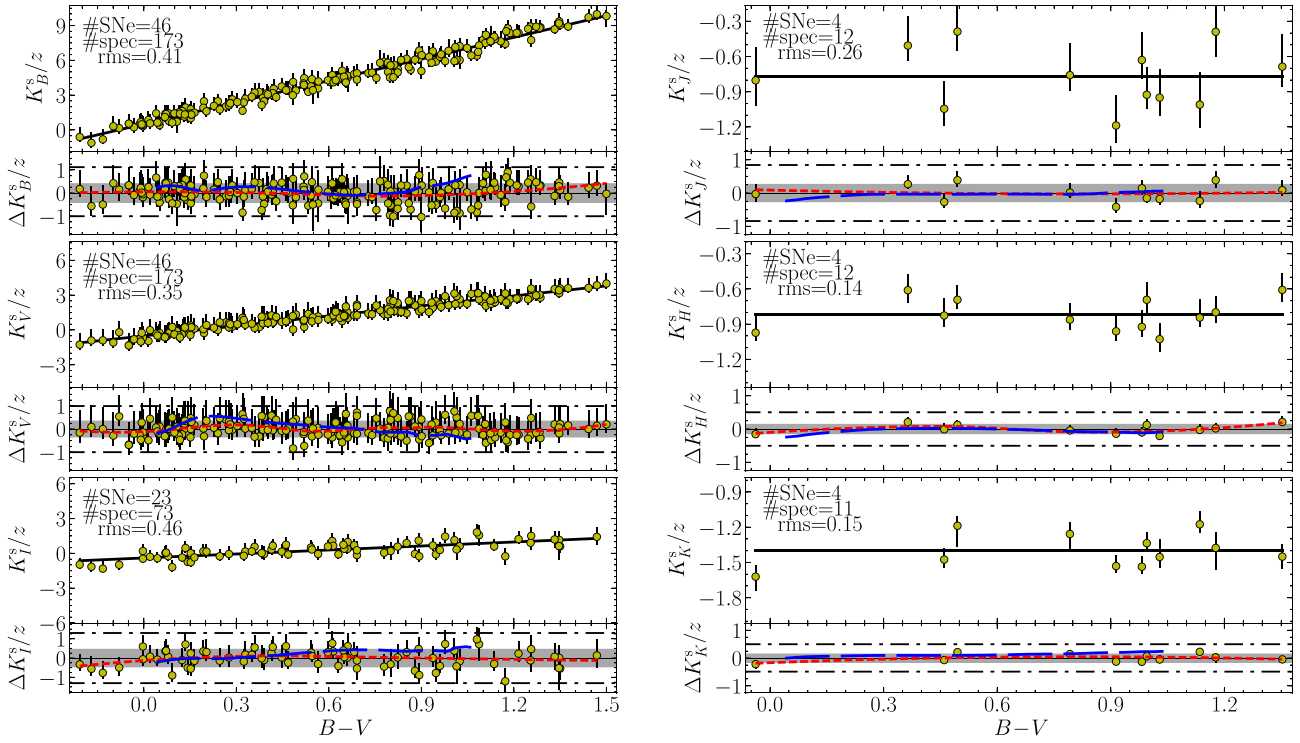

Figure 3. Selective term of the *K*-correction over redshift for *BVI* (left-hand side) and *JHK* (right-hand side) for SNe II as a function of the intrinsic *B–V* colour, along with residuals. Solid black lines correspond to the polynomial fits. Red short-dashed lines correspond to LOESS regressions to the residuals, while blue long-dashed lines correspond to residuals between the m15mlt3 model (Dessart et al. 2013) and polynomial fits from observations. Grey regions indicate values within one rms, while black dash-dotted lines are the inner fences.

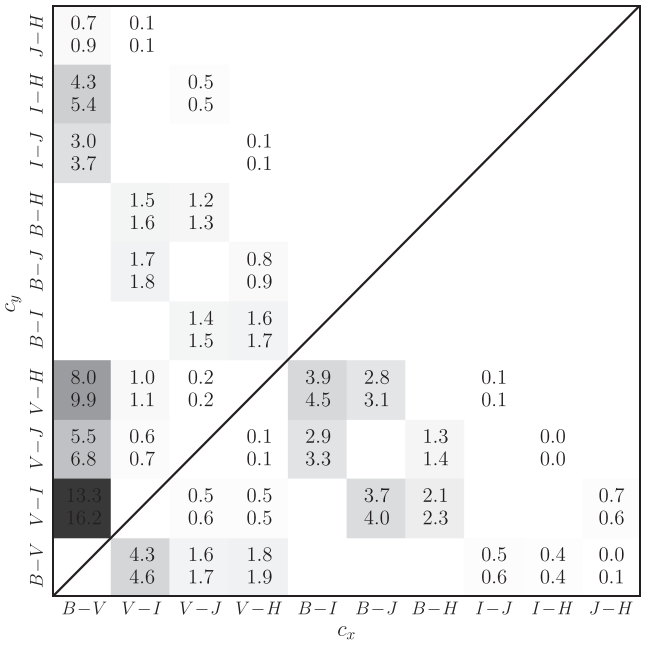

Figure 4. Values of $\xi_{S,i}$ for different combinations of c_x and c_y, using $B–V = 0.0$ (top values) and 1.4 (bottom values). Empty spaces indicate superfluous colour combinations.

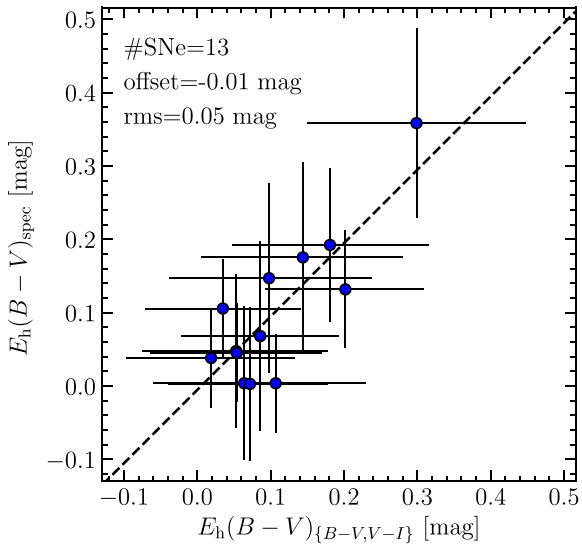

Figure 5. Comparison between $E_h(B–V)$ obtained with the spectrum-fitting method (*y*-axis) and those obtained with the *V–I* versus *B–V* C3 method (*x*-axis). Dashed line represents the one-to-one correlation, with a median offset of −0.01 mag.

To estimate $E_h(B–V)$, we use equation (14) and each point in the *V–I* versus *B–V* colour–colour plot. The pdf of $E_h(B–V)$ is obtained in a similar way than the pdf of $n_{S,zp}$, but maximizing the likelihood of a constant-only model. We include in the final pdf of $E_h(B–V)$ the error induced by errors on $n_{S,zp}$ and $M\{m_S\}$. Median values and errors of $E_h(B–V)$ are listed in Column 2 of Table F3. For our SN set we obtain $E_h(B–V)$ rms errors between 0.082 and 0.128 mag, with a median of 0.097 mag.

Fig. 5 shows the comparison between host galaxy colour excesses computed with $S = \{B–V, V–I\}$ with those obtained by Olivares E.

et al. (2010), $E_h(B–V)_{spec}$ (Column 5 of Table F3), which are based on the fit between observed spectra and SN II models. We measure a median offset of −0.01 mag, meaning that our estimations of $E_h(B–V)$ are slightly lower than those estimated by Olivares E. et al. (2010). Both methods are consistent within ±0.05 mag.

8 EXPLOSION EPOCH AND PHOTOSPHERIC VELOCITY

The explosion epoch and the photospheric velocity are, under the assumption of homologous expansion, the unique parameters determining the actual size of the photosphere (Kirshner & Kwan 1974).

8.1 Photospheric velocities

The most widely used method to estimate SN photospheric velocities consists of measuring the blueshift of P Cygni absorption minima in SN spectra (Kirshner & Kwan 1974; Eastman & Kirshner 1989). Weak lines, like those from Fe II species, are typically used under the assumption that they are formed near the photosphere (e.g. Leonard et al. 2002). A more confident method to estimate photospheric velocities is through the cross-correlation technique (Hamuy et al. 2001; Takáts & Vinkó 2012), where observed spectra are compared to those from SN models that have known photospheric velocities. The application of the latter method is beyond the scope of this work; therefore, we will use velocities derived from the Fe II λ5169 line absorption minima as a proxy for the photospheric velocity.

To estimate Fe II λ5169 absorption minima with appropriate errors, we have to consider the uncertainties induced by the noise and spectral resolution (Δλ) of each spectrum, and also by the endpoints we choose for the line profile.

We estimate the noise on the Fe II λ5169 line profile of each spectrum performing a LOESS fit and then removing it to the observed line profile. Then we generate 10^4 simulated line profiles, varying randomly the noise over the LOESS fit, wavelengths within Δλ, and endpoints. For each realization we apply a LOESS fit, registering the minimum value. The output of this process is a distribution of absorption minima, which we convert to velocities using the relativistic Doppler equation. With this process we obtain typical v_{ph} rms errors between 30 and 230 km s^{-1}, with a median of 76 km s^{-1}.

Photospheric velocities are estimated from spectroscopic data, corrected for the SN heliocentric redshift. In some cases, SN II spectra show narrow emission lines as a result of a superposed H II region at the SN position. These narrow lines allow a good estimation of the SN heliocentric redshift, under the assumption that the SN is spatially close to the H II region (e.g. Anderson et al. 2014a). When those lines are not present in the SN spectra, the heliocentric redshift of the host galaxy is used as a proxy for the SN heliocentric redshift. However, since most of the SNe II in our set explode in spiral galaxies, the SN heliocentric redshift has a component due to the galaxy rotation. Anderson et al. (2014a) computed heliocentric redshifts of 72 SNe II using H II region narrow emission lines, and comparing with heliocentric redshifts of the host galaxy nucleus, they obtained a zero-centred distribution with an rms of 162 km s^{-1}, which is attributed to the galaxy rotation effect.

In our sample, 11 SNe II (SN 2002gd, SN 2002gw, SN 2002hj, SN 2003B, SN 2003E, SN 2003bl, SN 2003bn, SN 2003ci, SN 2005ay, SN 2009N, and SN 2014G) show H II region narrow emission lines in the spectra, which we use to estimate the heliocentric redshift. Another six SNe (SN 2003T, SN 2004et, SN 2005cs, SN 2008in, SN 2012aw, and SN 2013ej) exploded within nearly face-on galaxies, in which case we adopt the redshift of the host galaxy nucleus. For SN 1999em we adopt the value from Leonard et al. (2002), and for SN 2003hn we use the average of the Na I D velocities measured by Sollerman et al. (2005). The remaining five SNe (SN 2003cn, SN 2009ib, SN 2009md, SN 2012A, and SN 2012ec) did not occur within nearly face-on galaxies, and do not show H II region narrow emission lines in the spectra. For those cases we adopt the redshift of the host galaxy nucleus, with an error of 162 km s^{-1} (that we assume normal) to take into account the host galaxy rotational velocity. Adopted SN heliocentric redshifts are listed in Table 1.

8.2 Explosion epoch

The SN explosion epoch can be estimated by means of photometric information; it can be constrained between the last non-detection t_{ln} and the first detection t_{fd} (e.g. Nugent et al. 2006; Poznanski et al. 2009; D'Andrea et al. 2010; R14; Valenti et al. 2016), or estimated through a polynomial fit to the rise-time photometry when it is available (e.g. Gall et al. 2015; González-Gaitán et al. 2015). The spectroscopy of an SN can also provide information about its explosion epoch by means of the comparison with other spectra of SNe with explosion epoch estimated through photometric information (e.g. Anderson et al. 2014b; Gutiérrez et al. 2017).

Columns 4 and 5 of Table F3 lists the t_{ln} and t_{fd} values of the SNe in our set, respectively. The explosion epochs for our set are typically constrained within 14 d using photometric information, which is twice the range suggested by R14 (namely, 7 d) to reduce errors induced by t_0 errors over PMM distances. We need, therefore, to include spectroscopic information in order to better constrain the explosion epochs.

As was done by Anderson et al. (2014b) and Gutiérrez et al. (2017), to estimate t_0 we use optical spectroscopy along with the Supernova Identificator code (SNID; Blondin & Tonry 2007), which finds by cross-correlation the spectra from its SN library that are more similar to the input spectrum. For a good estimation of t_0 with SNID, we need a library with spectra of an ample amount of SNe II that sample the high spectral diversity displayed by SNe II (e.g. Gutiérrez et al. 2017) and with t_0 constrained by photometric information. In this work, we compile optical spectroscopy of 59 SNe II with t_0 constrained within 10 d (for more details, see Appendix D).

To estimate the explosion epoch of a given SN (SN_{input}) with N spectra ({spec}) through SNID and using our SN II templates library, we perform the following procedure:

(1) We run SNID using as input the N spectra of SN_{input} earlier than 40 d since the first detection. The SNID output for each spectrum is a list with the best-matching templates, their phase since explosion, and their *r*lap parameter (which indicates the strength of the correlation).

(2) We convert phases since explosion to explosion epochs (since we know the phase of each SN_{input} spectrum). The associated errors are derived from the *r*lap values through a procedure described in Appendix D.

(3) From each of the N lists, we select the first 10 best-matching templates with *r*lap > 5.0, compiling them in a unique list. From this list, we extract a sublist for each of the M best-matching SNe (SN_{bm}). With each of the M sublist, we compute the SN_{in} explosion epoch as the average, taking the standard deviation as the associated error, and including the respective explosion epoch error of the SN_{bm} through a Monte Carlo error propagation. If a spectrum gives a median t_0 greater than 40 d, then we remove it from the analysis.

(4) After that, we compute the likelihood $\mathcal{L}(t_0|\{\text{spec}\})$ with the M results, including an error of 4.1 d which is the rms obtained from the comparison between explosion epochs constrained with photometric information and those derived with SNID (see Appendix D).

(5) Finally, we obtain the posterior pdf of t_0, $p(t_0|\{\text{spec}\})$, combining $\mathcal{L}(t_0|\{\text{spec}\})$ with the uniform prior on t_0, $p(t_0)$, provided by photometric information, i.e.

$$p(t_0|\{\text{spec}\}) \propto \mathcal{L}(t_0|\{\text{spec}\})p(t_0). \quad (18)$$

Table F3 lists the medians and rms values of the explosion epochs obtained with SNID and without any prior on t_0 (Column 7), and the median of $p(t_0|\{\text{spec}\})$ of each SN along with the 80 per cent CI (Column 8).

9 APPLYING THE PMM

Once all observables required for the PMM are available, the next step is to prepare the data before applying the method. As was mentioned in Section 4, we interpolate photometry to the epochs of the photospheric velocities. Since we want to study the PMM distance precision at different photometric bands, i.e. changing only the photometry, we use epochs where spectroscopy is covered simultaneously by optical and near-IR photometry. In the case of SN 2002hj, it does not have spectroscopy covered by *J*-band photometry, so we interpolate photospheric velocities (using LOESS) and *BVIH* photometry to the epochs of *J*-band photometry.

9.1 Calibration

For the PMM calibration, we express $a_{x,\Delta t}$ as

$$a_{x,\Delta t} = \text{ZP}_x + a^*_{x,\Delta t}, \quad (19)$$

where ZP_x is the zero-point of the PMM in the x-band, and $a^*_{x,\Delta t}$ is a function that represents the dependence of $a_{x,\Delta t}$ on Δt (without the constant term).

To estimate the evolution of $a^*_{x,\Delta t}$ with Δt, we use the $a^*_{x,\Delta t_i}$ values of the SNe in our set with two or more v_{ph} measurements during the photospheric phase. For each SN, the $a^*_{x,\Delta t_i}$ values are given by

$$a^*_{x,\Delta t_i} = m^{\text{corr}}_{x,i} + 5\log\left(\frac{v_{\text{ph},i}}{5000\ \text{km s}^{-1}}\right) + \delta_{\text{SN}}, \quad (20)$$

where δ_{SN} is an additive term to normalize the $a^*_{x,\Delta t_i}$ values of each SN to the same scale. Based on the definition given in R14, the dependence of $a^*_{x,\Delta t}$ on Δt has the form

$$a^*_{x,\Delta t} = f_{x,\Delta t} - 5\log\left(\frac{\Delta t}{100\ \text{d}}\right). \quad (21)$$

We express the dependence of $f_{x,\Delta t}$ on Δt through polynomials. We use the AIC/BIC to determine the optimum polynomial order for $f_{x,\Delta t}$ and the values of δ_{SN}, while to estimate the time range of applicability of the PMM, we group the $f_{x,\Delta t_i}$ values in bins of width 10 d and then we compute the rms of the points in each bin. We found that rms values are lower in a range 35–75 d since the explosion. Among all optimum orders for *BVIJH* bands (see Table F1), we select the order that the different bands have in common, i.e. order one. With this, we prevent that differences in the rms($f_{x,\Delta t}$) value for different bands are due to differences in the order of the polynomial fit. To estimate error in the parameters, we perform 10^4 bootstrap resampling. Table 2 lists $f_{x,\Delta t}$ fits parameters for *BVIJH* bands.

The left half of Fig. 6 shows the values of $a^*_{x,\Delta t_i}$ as a function of Δt_i for *BVIJH* bands. The variation of the LOESS fits (red dashed lines) are within one rms (black dotted lines), which means that polynomial fits we adopted capture almost all the dependence on Δt.

Table 2. Parameters for the PMM calibration.

	$f_{x,\Delta t} = c_x \cdot \Delta t/(100\ \text{d}^{-1})$			zero-point	
x	c_x	rms	p(RM)	ZP_x	rms
B	$3.87^{+0.32}_{-0.26}$	0.09	0.05	$-19.51^{+0.52}_{-0.52}$	0.27
V	$2.78^{+0.31}_{-0.22}$	0.09	0.32	$-20.03^{+0.39}_{-0.39}$	0.19
I	$2.22^{+0.34}_{-0.24}$	0.10	0.70	$-20.36^{+0.23}_{-0.23}$	0.15
J	$2.13^{+0.29}_{-0.27}$	0.10	0.51	$-20.64^{+0.12}_{-0.12}$	0.10
H	$2.05^{+0.28}_{-0.28}$	0.09	0.92	$-20.77^{+0.09}_{-0.09}$	0.07

Note: Parameters are valid for 35 d $< \Delta t <$ 75 d. Errors are the 99 per cent CI.

The PMM zero-points can be obtained using a sample of SNe II at known distances where, for each SN, we have

$$\text{ZP}^{\text{SN}}_x = \mu^*_x - \mu^{\text{SN}}_{\text{host}}. \quad (22)$$

Here, $\mu^{\text{SN}}_{\text{host}}$ is the SN host galaxy distance modulus and μ^*_x is the SN pseudo-distance modulus. The latter, for each measurement of v_{ph} at time t_i, is defined similar to equation (2) but with $a^*_{x,\Delta t_i}$ instead of $a_{x,\Delta t_i}$, i.e.

$$\mu^*_{x,i} = m^{\text{corr}}_{x,i} - a^*_{x,\Delta t_i} + 5\log\left(\frac{v_{\text{ph},i}}{5000\ \text{km s}^{-1}}\right). \quad (23)$$

The pdfs of $\mu^*_{x,i}$ are obtained through equation (23) using the pdfs of the observables for each photospheric velocity epoch. Finally, we combine the pdfs of $\mu^*_{x,i}$ in a unique μ^*_x pdf maximizing the likelihood (equation A1) for a constant-only model.

To compute accurate ZP_x values, we need SNe II in galaxies with distances measured with the best possible precision. Among the SNe that we compiled from the literature, there are only three (SN 1999em, SN 2003hn, and SN 2012aw) in galaxies with distances measured through Cepheid, and five (SN 2003hn, SN 2004et, SN 2005cs, SN 2012aw, and SN 2013ej) in galaxies with distances measured with TRGB. Cepheid distances for the hosts of SN 1999em and SN 2012aw were reported by Saha et al. (2006), while Riess et al. (2016) reported the Cepheid distance of the host of SN 2003hn. Comparing Cepheid distances of six galaxies in common between the two publications (NGC 1365, NGC 3370, NGC 3982, NGC 4536, NGC 4639, and NGC 5457) we found that Cepheid distances reported by Saha et al. (2006) are, on average, 0.19 mag greater than those reported by Riess et al. (2016), showing an rms of 0.13 mag. The latter could indicate a systematic difference between the two calibrations, which can introduce an undesirable noise on the ZP_x estimation if we rescale Saha et al. (2006) distances to the Riess et al. (2016) calibration. For this reason, we decide to use only SNe in galaxies with TRGB distances, that can be homogenized to the Jang & Lee (2017a) calibration, which is based on the distance to the Large Magellanic Cloud and NGC 4258. Recalibrated TRGB distances are listed in Column 6 of Table 1. From these five SNe II, we discard SN 2004et since the TRGB distance of its host is at least 0.59 mag higher compared to the distances we compute for SN 2004et and two other SNe II that exploded in the same galaxy (see Appendix E).

The right half of Fig. 6 shows the ZP^{SN}_x values for *BVIJH*. As in the case of μ^*_x, the pdf of ZP_x is obtained combining the pdfs of ZP^{SN}_x. Median values, 99 per cent CI, and rms values for ZP_x are summarized in Table 2.

Once the PMM zero-points are computed, we can estimate the distance modulus for each band as $\mu_x = \mu^*_x - \text{ZP}_x$. Median val-

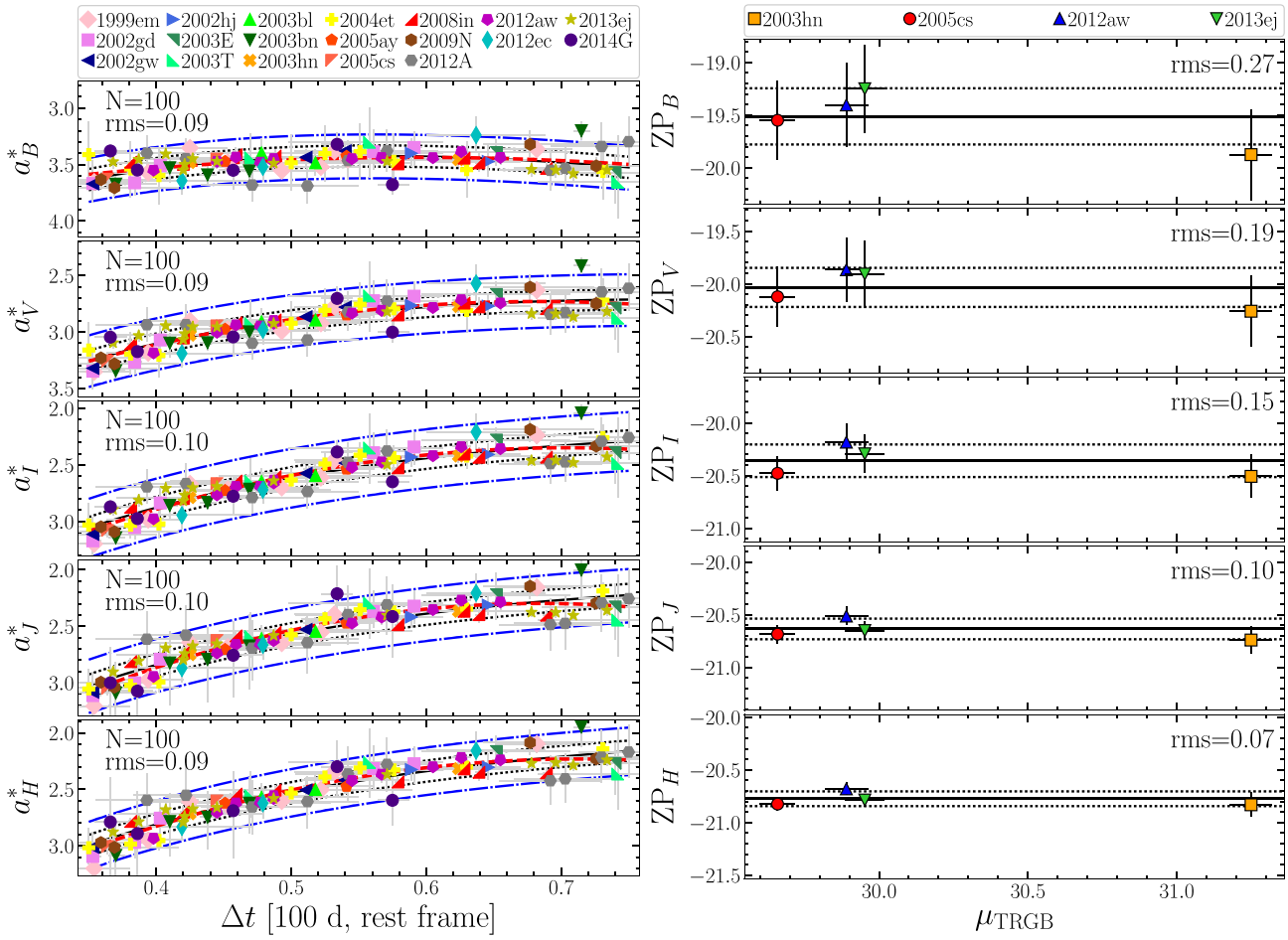

Figure 6. Left-hand panel: values of a^*_x as a function of Δt for *BVIJH*. Black solid lines correspond to the parametric fits. Red dashed lines correspond to LOESS regressions. Dotted lines indicate values within one rms, while blue dash-dotted lines are the inner fences. Right-hand panel: ZP_x values for *BVIJH* derived with four SNe II in galaxies with TRGB distances.

ues, 80 per cent CI, and rms values for μ_x are summarized in Table F4, where we include the TRGB zero-point systematic error of 0.058 mag (Jang & Lee 2017a).

9.2 Hubble diagrams

To investigate the PMM distance precision, we construct HDs. We convert heliocentric host galaxy redshifts to cosmological ones using as reference the cosmic microwave background (CMB) dipole (Fixsen et al. 1996). Redshift errors are dominated by peculiar velocities, with an rms of 382 km s^{-1} for local SN Ia host galaxies ($z <$ 0.08, Wang et al. 2006), followed by the error in the determination of the Local Group velocity (rms of 187 km s^{-1}, Tonry et al. 2000). CMB redshifts and their rms errors are listed in Table F4.

Taking into account the pdfs of the pseudo-distance moduli (μ^*_x) and the pdfs of the CMB redshifts ($cz_{\rm CMB}$), we compute the HD intercept ($a_{{\rm HD},x}$) maximizing the likelihood (equation A1), where the model for the pseudo-distance modulus is given by the Hubble law

$$\mu^*_x = a_{{\rm HD},x} + 5\log(cz_{\rm CMB}). \quad (24)$$

The left half of Fig. 7 shows HDs for *BVIJH* bands, using PMM distances for all SNe in our set. The rms, greater than 0.5 mag for all bands, is mostly produced by peculiar velocities of host galaxies at low redshift. In fact, the median redshift of the host galaxies in the HD is 1528 km s^{-1}, where a redshift error of 382 km s^{-1} translates into a magnitude error of 0.54 mag. Indeed, if we use redshifts corrected for the infall of the Local Group towards the Virgo cluster and the Great Attractor ($cz_{\rm corr}$) instead of CMB redshifts, we obtain an HD rms of 0.34–0.38 mag for *VIJH* bands (see the right half of Fig. 7). We note that even after infall corrections the scatter in the HDs is still mostly due to SNe in galaxies with $cz <$ 2000 km s^{-1}. Therefore, to estimate the PMM distance precision and the Hubble constant (H_0), given by

$$\log H_0 = (25 - a_{{\rm HD},x} + {\rm ZP}_x)/5, \quad (25)$$

we use only SNe II with $cz >$ 2000 km s^{-1} and, as visible in the left half of Fig. 8, the HD rms decreases significantly. The corresponding values of H_0 and rms are listed in Table 3.

The values of H_0 range between 67.1 and 74.9 km s^{-1} Mpc^{-1}. Taking into account that the ZP_x values were calibrated using TRGB distances in the scale of Jang & Lee (2017a), our H_0 values, as expected, are consistent within the errors with those reported in Jang & Lee (2017b), i.e. 71.17 ± 1.66 ± 1.87 km s^{-1} Mpc^{-1}, which also use the Jang & Lee (2017a) calibration.

As visible in Column 4 of Table 3, all the H_0 values are compatible within their errors. However, we note that H_0 decreases moving from shorter to longer wavelengths, which could suggest a system-

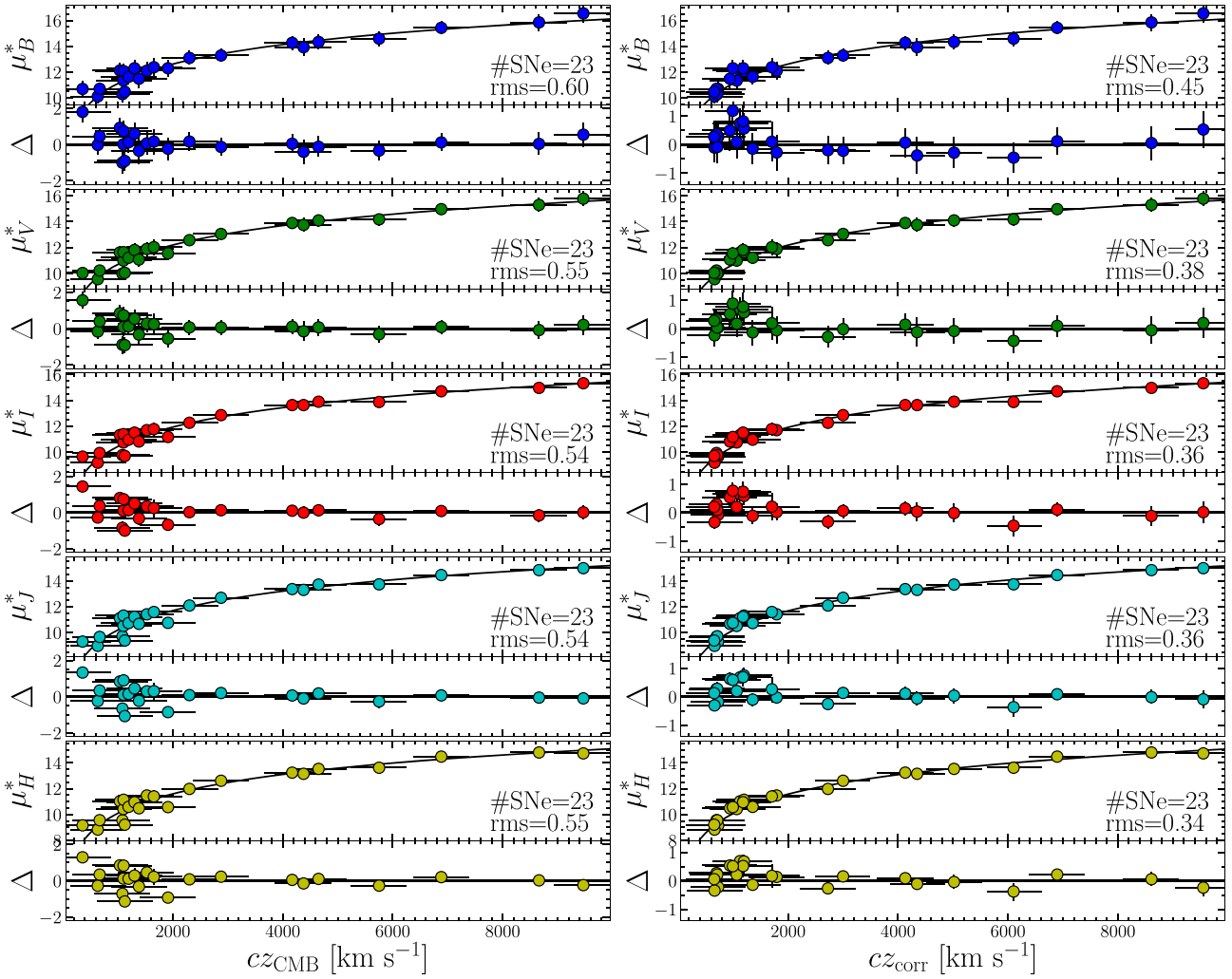

Figure 7. Hubble diagrams for SNe II with PMM distances and CMB redshifts (left-hand panel) and redshifts corrected for the Virgo and Great Attractor infall (right-hand panel). Solid lines correspond to Hubble law fits. Residuals are plotted at bottom of each panel.

atic introduced by: (1) our assumption of the R_V value for the SN host galaxies, or (2) an underestimation and/or an overestimation of the host galaxy colour excesses for the four SNe in the PMM calibration set and the nine SNe at $cz_{\rm CMB} > 2000\,{\rm km\,s^{-1}}$, respectively. To test the first possibility, we change the R_V adopted for SN II host galaxies to the lowest R_V value for which the Fitzpatrick (1999) extinction curve is defined ($R_V = 2.3$). As is visible in Column 6 of Table 3, there are no significant changes in the H_0 values. For the second possibility, we found that an underestimation of $E_{\rm h}(B–V)$ for the SNe in the calibration set, or an overestimation of $E_{\rm h}(B–V)$ for the SNe at $cz_{\rm CMB} > 2000\,{\rm km\,s^{-1}}$, of 0.05–0.07 mag can erase the tension between the H_0 values for all bands. Given the typical statistical $E_{\rm h}(B–V)$ error of 0.097 mag (see Section 7), the probability of obtaining an $E_{\rm h}(B–V)$ underestimation of 0.05–0.07 mag with four objects is of 8 per cent, while to obtain an overestimation in a same amount for nine objects is of 5 per cent. It is worth mentioning also that the scatter in ZP_x decreases going from shorter to longer wavelengths, suggesting again a trend introduced by the combination of a large uncertainty in the colour excess estimation and the low number statistics.

Regarding the HD scatter, we note that the rms of 0.28 mag obtained with the *B*-band decreases to 0.15–0.18 mag for the *VIJH* bands. Despite the good results, the low number of SNe II within galaxies at $cz_{\rm CMB} > 2000\,{\rm km\,s^{-1}}$ makes the result not statistically robust. Therefore, to check the PMM distance precision, it is necessary to include more SNe II into the analysis. Thus, we include the four SNe II used for the PMM calibration, plus other two in galaxies having Cepheid and SN Ia distances. The latter distances are converted to redshifts through the Hubble law (equation 24), where for each band we use the H_0 value listed in Column 4 of Table 3 and the ZP value given in Table 2.

The right half of Fig. 7 shows the HDs computed with the selected SNe II based on the aforementioned criterion, which correspond to our final sample. For *VI* bands we obtain an HD rms of 0.15–0.16 mag. The lowest HD rms is obtained with the *J*-band, whose rms of 0.13 mag translates into a distance precision of 6 per cent. This value, compared to the rms of 0.15–0.26 mag obtained for optical bands, suggests that using the *J*-band photometry instead of optical one to measure PMM distances can improve the precision by at least 0.07 mag.

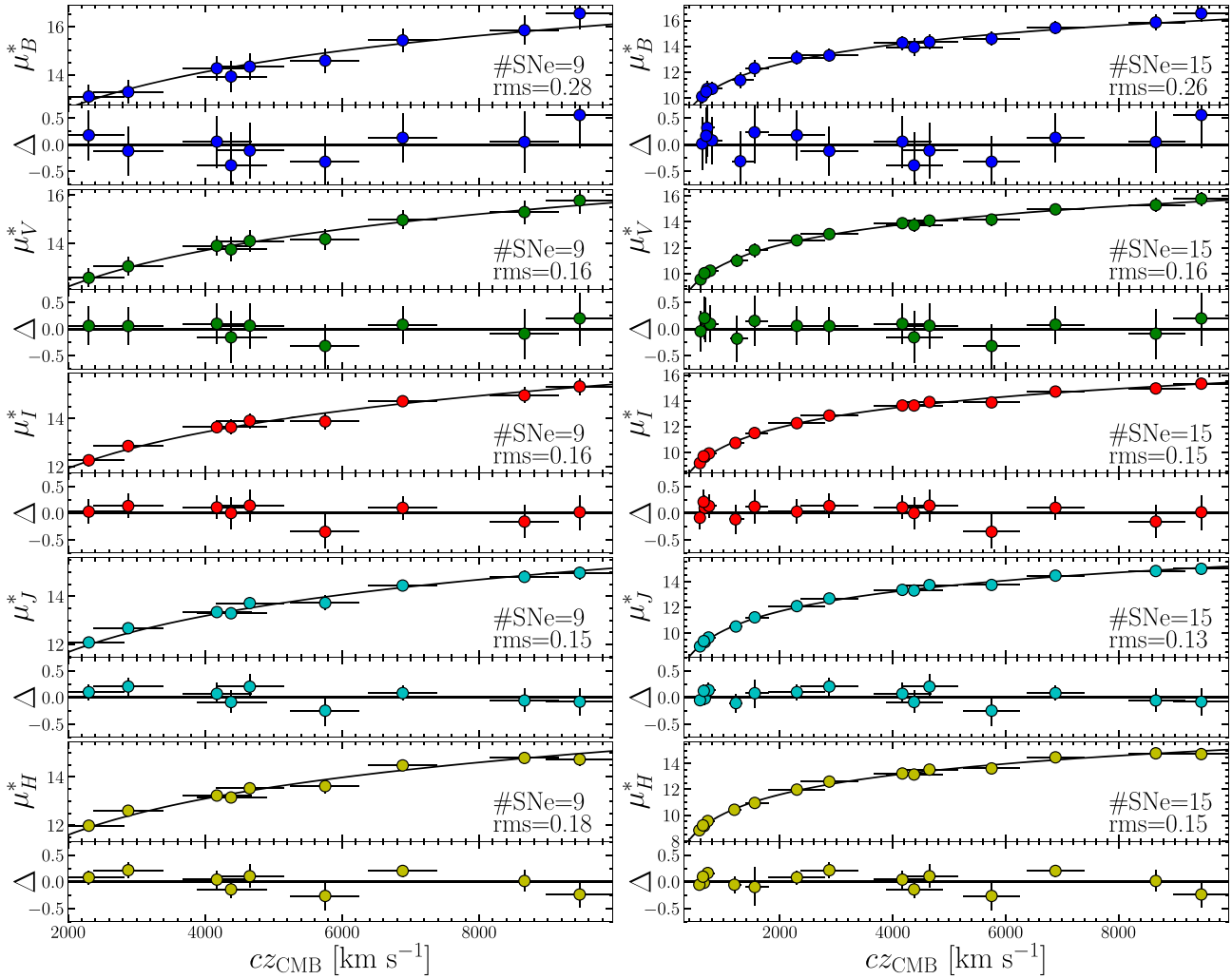

Figure 8. Hubble diagrams for SNe II with distances computed with the PMM, using the nine SNe II at $cz > 2000\,\mathrm{km\,s^{-1}}$ (left-hand panel) and including the six SNe II in galaxies with distance measured with TRGB, Cepheids, or SN Ia (right-hand panel), where the H_0 values are those computed with the nine SNe II at $cz > 2000\,\mathrm{km\,s^{-1}}$, and used to convert distances of the six nearest SNe II to redshifts. Solid lines correspond to the Hubble law fits. Residuals are plotted at the bottom of each panel.

For the *H*-band we expected a similar HD rms than for *J*-band since, among *BVIJH* bands, the *H*-band is the least affected by dust extinction. We, however, obtained an HD rms of 0.15 mag. The latter can be partially due to the higher photometry error of the *H*-band (of 0.07 mag) with respect to the error of the *J*-band (of 0.05 mag).

10 DISCUSSION

10.1 Statistical significance of the result

Given the small size of our SN sample, the HD rms of 0.13 mag we measured for the *J*-band is not statistically robust enough to be considered as a measure of the PMM distance precision in that band. In particular, we want to know the probability of measuring an rms $\leq$0.13 mag with $N = 15$ values drawn from a parent distribution with standard deviation (σ) $\geq$ 0.13 mag. Assuming a normal parent distribution, the quantity $(N-1)(\mathrm{rms}/\sigma)^2$ has a chi-square distribution with $N-1$ degrees of freedom. Using this, we found that there is a 1 per cent chance that the parent distribution has $\sigma = 0.23$ mag. Therefore, with the evidence we have, we can set an upper limit on the PMM distance precision with the *J*-band of 10 per cent with a CL of 99 per cent.

10.2 Comparison with other methods

For a consistent comparison of our results with those from other SN II distance measurement methods, we select results from works that uses a sample of SNe II at $z \approx 0.01$–0.03.

Table 4 lists the best distance precisions reached by other SN II distance measurement methods along with results obtained in this work. We note that the precision we report in this work is significantly lower than the best dispersion obtained by other works with SCM and PCM.

We also compare PMM and SCM applied to the same sample for *J*- and *H*-band. For this comparison we discard SN 2002hj because

Table 3. Hubble diagram parameters.

	All[a]		$cz_{CMB} > 2000\,km\,s^{-1}$				Final[d]
	cz_{CMB}	cz_{corr}	$R_V = 3.1$[b]		$R_V = 2.3$[b]		
Band	rms	rms	H_0[c]	rms	H_0[c]	rms	rms
B	0.60	0.45	$74.9^{+10.6}_{-9.2}$	0.28	$75.8^{+11.0}_{-9.6}$	0.30	0.26
V	0.55	0.38	$71.4^{+8.2}_{-7.3}$	0.16	$71.5^{+7.9}_{-7.1}$	0.16	0.16
I	0.54	0.36	$69.5^{+6.7}_{-6.1}$	0.16	$69.4^{+6.4}_{-5.8}$	0.16	0.15
J	0.54	0.36	$68.6^{+5.7}_{-5.2}$	0.15	$68.7^{+5.7}_{-5.2}$	0.15	0.13
H	0.55	0.34	$67.1^{+5.4}_{-5.0}$	0.18	$67.2^{+5.4}_{-5.0}$	0.18	0.15

[a]We do not report the H_0 values for this SN set because they are severely affected by peculiar velocities.
[b]R_V value adopted for SN II host galaxies.
[c]In $km\,s^{-1}\,Mpc^{-1}$. Errors are the 80 per cent CI, and include the TRGB zero-point systematic error and the error in the determination of the Local Group velocity.
[d]Set of 15 SNe II: nine SNe at $cz_{CMB} > 2000\,km\,s^{-1}$ plus six SNe in galaxies with TRGB, Cepheids, or SN Ia distances.

Table 4. Distance precision of different methods.

Method	HD rms	Band	#SNe	Reference
PCM	0.43	*Y*	30	de Jaeger et al. (2015)
SCM	0.25	*B*	19	Olivares E. et al. (2010)
PMM	0.13	*J*	15	This work
PMM[a]	0.14	*J*	14	This work
PMM[a]	0.14	*H*	14	This work
SCM[a,b]	0.21	*J*	14	This work
SCM[a,b]	0.23	*H*	14	This work

[a]Excluding SN 2002hj from the SN sample.
[b]Using the PMM parameters evaluated at 50 d.

Table 5. Error budget for the PMM *J*-band distances.

Error source	Typical error	Error on μ_J (mag)	Per cent of total error
$E_h(B–V)$	0.097 mag	0.079	35.7
t_0	2.6 d	0.066	24.9
ZP_J	0.050 mag[a]	0.050	14.3
m_J	0.049 mag	0.049	13.7
v_{ph}	$60\,km\,s^{-1}$	0.040	9.2
cz_{hel}	$29\,km\,s^{-1}$	0.019	2.1
K_J	0.003 mag	0.003	0.05
$E_G(B–V)$	0.004 mag	0.003	0.05
	Total	0.132	100.0

[a]It does not include the TRGB zero-point systematic error.

there is not photometry in *J*-band at 50 d since explosion. As visible in Table 4, the dispersion is lower by ∼30–40 per cent in both band.

10.3 Error budget

Taking into account that the lowest HD rms is obtained with the *J*-band, in Table 5 we show the statistical error budget for the distances measured for that band. We see that 88.6 per cent of the statistical error is induced by the errors of the first four terms: the host galaxy colour excess, the explosion epoch, the PMM zero-point, and the *J*-band photometry. Therefore, it is possible to improve the performance of the PMM in the future developing a better method to estimate $E_h(B–V)$, selecting SNe II with explosion epoch constrained within a small range of time, including more SNe II in the PMM calibration set, and increasing the quality of the *J*-band photometry.

10.4 Diminishing systematics

Our results show that we are reaching a precision in distance modulus of ±0.1 mag with the PMM at near-IR wavelengths. Therefore it is important to control systematics, and push them below 0.1 mag. For the latter in the following, we analyse sources of systematics affecting our results:

(1) Explosion epoch: The dependence of the PMM calibration on explosion epoch (left half of Fig. 6) is stronger at early times, so t_0 errors have a strong effect at those epochs. In order to obtain errors lower than 0.1 mag for observations at $\Delta t \gtrsim 35$ d, we need SNe II with explosion epochs constrained within 5 d.

(2) SN heliocentric redshift: When the host galaxy heliocentric redshift is used as a proxy of the SN heliocentric redshift, a systematic error of

$$\sigma(M_{x,\Delta t_i,v_{ph,i}}) = \frac{5}{\ln 10}\frac{162\ km\ s^{-1}}{v_{ph,i}} \quad (26)$$

is introduced into the absolute magnitude (equation 1). This effect increases when the photospheric velocity decreases, translating into errors $\gtrsim 0.1$ mag for photospheric velocities $\lesssim 3500\,km\,s^{-1}$. Therefore, if optical spectra of an SN II do not show H II narrow emission lines due to a nearby H II region or if the SN is not within a nearly face-on galaxy, then epochs for which photospheric velocities are greater than $3500\,km\,s^{-1}$ are preferable.

(3) Host galaxy redshift: A galaxy is believed to be within the Hubble flow when its redshift is greater than 0.01. At that redshift, peculiar velocities are thought to be negligible compared with the velocities due to the Universe expansion. However, the typical error of $382\,km\,s^{-1}$ translates into a distance modulus error of 0.28 mag for $z = 0.01$. Including the error in the determination of the Local Group velocity of $187\,km\,s^{-1}$, the redshift error increases to $425\,km\,s^{-1}$. Therefore, in order to reduce the error induced by redshift errors at a level lower than 0.1 mag, it is necessary to observe SNe II within galaxies at $z > 0.03$.

11 CONCLUSIONS

Our main results are the following:

(1) Using nine SNe II at $cz > 2000\,km\,s^{-1}$, we obtained H_0 ranging between 67.1 and $74.9\,km\,s^{-1}\,Mpc^{-1}$, and an HD rms of 0.15–0.28 mag.

(2) Adding six SNe II with host galaxy distances measured with TRGB, Cepheids, or SN Ia (total 15), which distances were converted to redshifts through the Hubble law, we obtain an HD rms of 0.15–0.26 mag in the optical bands, which reduces to 0.13 mag in the *J*-band.

In order to test further the promising results we are obtaining in this work, it is necessary to carry out an optical and near-IR photometric follow-up of SNe II at $z > 0.03$ and with explosion epochs constrained within 5 d. For these SNe, it is necessary to take at least one optical spectrum at any epoch between 35 and 75 d since explosion.

It is evident from Fig. 1 that the quality of the near-IR photometry used in this work is, in general, lower than the optical one. Therefore,

we expect that increasing the quality of the near-IR photometry will further improve our results.

ACKNOWLEDGEMENTS

The authors thank the anonymous referee for the useful comments that helped to improve the original manuscript. OR, GP, AC, and YA acknowledge support by the Ministry of Economy, Development, and Tourism's Millennium Science Initiative through grant IC120009, awarded to The Millennium Institute of Astrophysics, MAS. OR acknowledges support from CONICYT PAI/INDUSTRIA 79090016. This research has made use of the NASA/IPAC Extragalactic Database (NED) which is operated by the Jet Propulsion Laboratory, California Institute of Technology, under contract with the National Aeronautics and Space Administration. This work has made use of the Weizmann Interactive Supernova Data Repository (https://wiserep.weizmann.ac.il).

This paper includes data gathered with the 6.5-m Magellan Telescopes located at Las Campanas Observatory, Chile.

REFERENCES

Akaike H., 1974, IEEE Trans. Autom. Control, 19, 716
Akaike H., 1978, J. Royal Stat. Soc. Series D, 27, 217
Anand G. S., Rizzi L., Tully R. B., 2018, AJ, 156, 105
Anderson J. P. et al., 2014a, MNRAS, 441, 671
Anderson J. P. et al., 2014b, ApJ, 786, 67
Anderson J. P. et al., 2016, A&A, 589, A110
Barbarino C. et al., 2015, MNRAS, 448, 2312
Blondin S., Tonry J. L., 2007, ApJ, 666, 1024
Bohlin R. C., Gilliland R. L., 2004, AJ, 127, 3508
Bose S. et al., 2013, MNRAS, 433, 1871
Bose S. et al., 2015, ApJ, 806, 160
Bose S., Kumar B., 2014, ApJ, 782, 98
Brown P. J. et al., 2010, ApJ, 721, 1608
Burnham K. P., Anderson D. R., 2002, Model Selection and Multimodel Inference. 2nd edn, Springer-Verlag, New York
Cardelli J. A., Clayton G. C., Mathis J. S., 1989, ApJ, 345, 245
Childress M. J. et al., 2016, Publ. Astron. Soc. Aust., 33, e055
Cleveland W. S., Grosse E., Shyu W. M., 1992, in Chambers J. M., Hastie T. J., eds, Statistical models in S. Chapman and Hall, London, p. 309
Cohen M., Walker R. G., Carter B., Hammersley P., Kidger M., Noguchi K., 1999, AJ, 117, 1864
D'Andrea C. B. et al., 2010, ApJ, 708, 661
Dall'Ora M. et al., 2014, ApJ, 787, 139
Das K. R., Imon A. H. M. R., 2016, Am. J. Theor. Appl. Stat., 5, 5
de Jaeger T. et al., 2015, ApJ, 815, 121
de Jaeger T. et al., 2017a, MNRAS, 472, 4233
de Jaeger T. et al., 2017b, ApJ, 835, 166
Dessart L. et al., 2008, ApJ, 675, 644
Dessart L. et al., 2014, MNRAS, 440, 1856
Dessart L., Hillier D. J., 2005, A&A, 437, 667
Dessart L., Hillier D. J., Waldman R., Livne E., 2013, MNRAS, 433, 1745
Dhungana G. et al., 2016, ApJ, 822, 6
Doane D., Seward L., 2016, Applied Statistics in Business and Economics, 5th edn, McGraw-Hill, New York
Dwek E. et al., 1983, ApJ, 274, 168
Eastman R. G., Kirshner R. P., 1989, ApJ, 347, 771
Eastman R. G., Schmidt B. P., Kirshner R., 1996, ApJ, 466, 911
Elmhamdi A. et al., 2003, MNRAS, 338, 939
Faran T. et al., 2014a, MNRAS, 442, 844
Faran T. et al., 2014b, MNRAS, 445, 554
Filippenko A. V., 1982, PASP, 94, 715
Fitzpatrick E. L., 1999, PASP, 111, 63
Fixsen D. J., Cheng E. S., Gales J. M., Mather J. C., Shafer R. A., Wright E. L., 1996, ApJ, 473, 576
Fraser M. et al., 2011, MNRAS, 417, 1417
Fukugita M., Ichikawa T., Gunn J. E., Doi M., Shimasaku K., Schneider D. P., 1996, AJ, 111, 1748
Gal-Yam A. et al., 2008, ApJ, 685, L117
Gal-Yam A. et al., 2011, ApJ, 736, 159
Galbany L. et al., 2016, AJ, 151, 33
Gall E. E. E. et al., 2015, A&A, 582, A3
Gall E. E. E. et al., 2018, A&A, 611, A25
Gall E. E. E., Kotak R., Leibundgut B., Taubenberger S., Hillebrandt W., Kromer M., 2016, A&A, 592, A129
González-Gaitán S. et al., 2015, MNRAS, 451, 2212
Gutiérrez C. P. et al., 2017, ApJ, 850, 89
Hamuy M. et al., 2001, ApJ, 558, 615
Hamuy M., Pinto P. A., 2002, ApJ, 566, L63
Hamuy M. A., 2001, PhD thesis. Univ. Arizona
Harutyunyan A. H. et al., 2008, A&A, 488, 383
Hatt D. et al., 2018, ApJ, 866, 145
Hicken M. et al., 2017, ApJS, 233, 6
Hurvich C. M., Simonoff J. S., Tsai C.-L., 1998, J. Royal Stat. Soc. Series B, 60, 271
Imon A. H. M. R., 2003, Commun. Stat. Theor. Meth., 32, 1021
Inserra C. et al., 2013, A&A, 555, A142
Jang I. S., Lee M. G., 2017a, ApJ, 835, 28
Jang I. S., Lee M. G., 2017b, ApJ, 836, 74
Jarque C. M., Bera A. K., 1987, Int. Stat. Rev., 55, 163
Jones M. I. et al., 2009, ApJ, 696, 1176
Kasen D., Woosley S. E., 2009, ApJ, 703, 2205
Kirshner R. P., Kwan J., 1974, ApJ, 193, 27
Krisciunas K. et al., 2009, AJ, 137, 34
Leonard D. C. et al., 2002, PASP, 114, 35
Liddle A. R., 2007, MNRAS, 377, L74
Maguire K. et al., 2010b, MNRAS, 404, 981
Maguire K., Kotak R., Smartt S. J., Pastorello A., Hamuy M., Bufano F., 2010a, MNRAS, 403, L11
McQuinn K. B. W., Skillman E. D., Dolphin A. E., Berg D., Kennicutt R., 2017, AJ, 154, 51
Munari U., Carraro G., 1996, A&A, 314, 108
Murphy J. W., Khan R., Williams B., Dolphin A. E., Dalcanton J., Díaz-Rodríguez M., 2018, ApJ, 860, 117
Natali F., Natali G., Pompei E., Pedichini F., 1994, A&A, 289, 756
Nugent P. et al., 2006, ApJ, 645, 841
Olivares E. F. et al., 2010, ApJ, 715, 833
Olivares F., MSc thesis, Univ. de Chile, 2008, preprint (arXiv:0810.5518)
Pastorello A. et al., 2004, MNRAS, 347, 74
Pastorello A. et al., 2006, MNRAS, 370, 1752
Pastorello A. et al., 2009, MNRAS, 394, 2266
Pejcha O., Prieto J. L., 2015, ApJ, 799, 215
Poznanski D. et al., 2009, ApJ, 694, 1067
Poznanski D., Prochaska J. X., Bloom J. S., 2012, MNRAS, 426, 1465
Pozzo M. et al., 2006, MNRAS, 368, 1169
Quimby R. M., Wheeler J. C., Höflich P., Akerlof C. W., Brown P. J., Rykoff E. S., 2007, ApJ, 666, 1093
Rana M. S., Midi H., Imon A. H. M. R., 2009, J. Math. Stat., 5, 54
Riess A. G. et al., 2016, ApJ, 826, 56
Rizzi L., Tully R. B., Makarov D., Makarova L., Dolphin A. E., Sakai S., Shaya E. J., 2007, ApJ, 661, 815
Rodríguez Ó., Clocchiatti A., Hamuy M., 2014, AJ, 148, 107
Roy R. et al., 2011, ApJ, 736, 76
Saha A., Thim F., Tammann G. A., Reindl B., Sandage A., 2006, ApJS, 165, 108
Sahu D. K., Anupama G. C., Srividya S., Muneer S., 2006, MNRAS, 372, 1315
Sako M., et al., 2018, PASP, 130, 064002
Sanders N. E. et al., 2015, ApJ, 799, 208
Schlafly E. F. et al., 2016, ApJ, 821, 78
Schlafly E. F., Finkbeiner D. P., 2011, ApJ, 737, 103
Schlegel D. J., Finkbeiner D. P., Davis M., 1998, ApJ, 500, 525
Schmidt B. P. et al., 1993, AJ, 105, 2236

Schmidt B. P., Kirshner R. P., Eastman R. G., 1992, ApJ, 395, 366
Schmidt B. P., Kirshner R. P., Eastman R. G., Phillips M. M., Suntzeff N. B., Hamuy M., Maza J., Aviles R., 1994, ApJ, 432, 42
Schwarz G., 1978, Ann. Stat., 6, 461
Shapiro S. S., Wilk M. B., 1965, Biometrika, 52, 591
Shivvers I. et al., 2017, PASP, 129, 054201
Silverman J. M. et al., 2012, MNRAS, 425, 1789
Sollerman J., Cox N., Mattila S., Ehrenfreund P., Kaper L., Leibundgut B., Lundqvist P., 2005, A&A, 429, 559
Spiro S. et al., 2014, MNRAS, 439, 2873
Stritzinger M. et al., 2002, AJ, 124, 2100
Sugiura N., 1978, Commun. Stat. Theory Methods, 7, 13
Takáts K. et al., 2014, MNRAS, 438, 368
Takáts K. et al., 2015, MNRAS, 450, 3137
Takáts K., Vinkó J., 2012, MNRAS, 419, 2783
Terreran G. et al., 2016, MNRAS, 462, 137
Thompson L. A., 1982, ApJ, 257, L63
Tikhonov N. A., 2014, Astron. Lett., 40, 537
Tomasella L. et al., 2013, MNRAS, 434, 1636
Tomasella L. et al., 2018, MNRAS, 475, 1937
Tonry J. L., Blakeslee J. P., Ajhar E. A., Dressler A., 2000, ApJ, 530, 625
Tukey J. W., 1977 , Exploratory Data Analysis, Addison-Wesley, Reading
Valenti S. et al., 2014, MNRAS, 438, L101
Valenti S. et al., 2015, MNRAS, 448, 2608
Valenti S. et al., 2016, MNRAS, 459, 3939
Wagoner R. V., 1981, ApJ, 250, L65
Wang L., Strovink M., Conley A., Goldhaber G., Kowalski M., Perlmutter S., Siegrist J., 2006, ApJ, 641, 50
Yaron O. et al., 2017, Nat. Phys., 13, 510
Yuan F. et al., 2016, MNRAS, 461, 2003
Zhang J. et al., 2014, ApJ, 797, 5

SUPPORTING INFORMATION

Supplementary data are available at *MNRAS* online.

Please note: Oxford University Press is not responsible for the content or functionality of any supporting materials supplied by the authors. Any queries (other than missing material) should be directed to the corresponding author for the article.

Figure S1: Akaike and Bayesian weights, and evidence ratios for $R_x^{\rm G}$, $K_x^{\rm s}/z$, $R_x^{\rm h}$, and $f_{x,\,\Delta t}$.
Figure S2: SN II parameters.
Figure S3: CMB redshifts and PMM distance moduli.
Figure S4: SNII spectra library.
Figure S5: SNID templates.

APPENDIX A: MODEL SELECTION

For the model selection we consider two criteria: the 'an information criterion' (AIC, Akaike 1974), which is based on information theory, and the BIC (Schwarz 1978), which is based on Bayesian inference. From a set of R models, the AIC selects the model that have the least information loss with respect to the unknown true model, while the BIC selects the model with the highest likelihood $\mathcal{L}$, given by

$$\mathcal{L}(\text{model}|\{X_i\}) = \prod_{i=1}^{N} p(X_i|\text{model}). \tag{A1}$$

Here, X_i is the i-th observed data, $p(X_i|\text{model})$ is the probability density function (pdf) of X_i given the model, and N is the number of observed data points. Quantitatively, the AIC and BIC search for a balance between overfitting and underfitting penalizing the likelihood. For the AIC and the BIC, the best model is one that minimizes the quantity

$$\text{AIC} \equiv -2\ln\mathcal{L}_{\max} + 2Nk/(N-k-1) \tag{A2}$$

(corrected for small sample sizes, Sugiura 1978), and

$$\text{BIC} \equiv -2\ln\mathcal{L}_{\max} + k\ln N \tag{A3}$$

(Schwarz 1978), respectively, where $\mathcal{L}_{\max}$ is the maximum likelihood achievable by the model, and k is the number of parameters of the model.

It is known that a model selection based only on the minimum AIC value reached for a certain model does not provide enough evidence to prefer that model over the other ones (e.g. Akaike 1978; Burnham & Anderson 2002). Instead, it is necessary to include into the analysis the strength of evidence in favour of each model. To quantify the latter, it has been proposed to use the likelihood of the model given the data (e.g. Akaike 1978) which, normalized by the sum of likelihoods of all R models, defines the Akaike weights

$$w_i = \frac{e^{-0.5(\text{AIC}_i - \text{AIC}_{\min})}}{\sum_{r=1}^{R} e^{-0.5(\text{AIC}_r - \text{AIC}_{\min})}} \tag{A4}$$

(e.g. Burnham & Anderson 2002). Here, $\text{AIC}_{\min}$ is the minimum AIC value reached among the R models used in the analysis. The same idea is applicable for the BIC (Burnham & Anderson 2002), which defines the Bayesian weights

$$\text{P}_i = \frac{e^{-0.5(\text{BIC}_i - \text{BIC}_{\min})}}{\sum_{r=1}^{R} e^{-0.5(\text{BIC}_r - \text{BIC}_{\min})}}. \tag{A5}$$

For the AIC and BIC, the evidence ratios defined as w_i/w_j and p_i/p_j, respectively, allow comparison of the evidence in favour of the ith model as the best model versus the jth model. As reference, if evidence ratios are greater than 13.0, then there is a strong evidence in favour of the ith model over the jth model (e.g. Liddle 2007). If several models have substantial support as the best (e.g. evidence ratios $<$13.0), then, by the principle of parsimony, we select the one with less parameters.

In the case of least-square regressions, with random errors normally distributed and with constant variance,

$$-2\ln\mathcal{L}_{\max} = N\ln 2\pi\hat{\sigma}^2 + N \tag{A6}$$

(e.g. Burnham & Anderson 2002, p. 17), where $\hat{\sigma}^2$ is the average of squared residuals around the model. The AIC and BIC in this case can be expressed as

$$\text{AIC} = \ln\hat{\sigma}^2 + (N+k-1)/(N-k-1), \tag{A7}$$

$$\text{BIC} = \ln\hat{\sigma}^2 + k/N\cdot\ln N. \tag{A8}$$

Since $\hat{\sigma}^2$ is computed from data, it must be considered as a model parameter.

In the case of non-parametric regressions (NPR), like LOESS, k is not defined. Instead, it has been proposed to use the trace of the smoother matrix, tr(H), which is a quantity analogous to the number of parameters in a parametric regression (Cleveland et al. 1992; Hurvich, Simonoff & Tsai 1998). Replacing $k = \text{tr}(H) + 1$ in equation (A7) allows us to obtain the AIC version for NPR presented by Hurvich et al. (1998).

To check the normality of random errors, it is necessary to carry out a normality test. As we do not measure random errors directly, we use residuals instead. However, widely used normality tests like the Shapiro & Wilk (1965) and the Jarque & Bera (1987) test, when applied over residuals, have little power to reject the null hypothesis even when the random errors are not normal (Das & Imon 2016). Imon (2003) proposed a statistic more suitable to verify normality for regressions, which is based on the Jarque & Bera (1987) test and on the use of unbiased moments. The statistic of the test, called

Rescaled Moment (RM), is defined as

$$\mathrm{RM} \equiv Nc^3 \left[\hat{\mu}_3^2/\hat{\mu}_2^3/6 + c \cdot (\hat{\mu}_4/\hat{\mu}_2^2 - 3)^2/24\right] \quad \text{(A9)}$$

(Rana, Midi & Imon 2009), where $\hat{\mu}_i$ is the ith sample moment, and $c \equiv N/(N-k)$. Under the null hypothesis of a normal distribution, the RM statistic is asymptotically distributed as a chi-square distribution with two degrees of freedom.

APPENDIX B: SN II SPECTRA LIBRARY

In order to compute total-to-selective broad-band extinction ratios (Section 5 and 7) and K-corrections (Section 6) for SNe II, it is necessary to know their SED. The latter can be estimated through theoretical models (e.g. Sanders et al. 2015; de Jaeger et al. 2015, 2017b) or, as in Olivares (2008) and in this work, through spectroscopic observations.

In practice, spectra are not always taken with the slit oriented along the parallactic angle (PA), so their shape can be modified due to differential refraction (Filippenko 1982). Even when the slit is oriented along the PA, contamination due to the light from the host galaxy can produce spurious SEDs. Therefore we have to check the flux calibration of spectra before using them as proxies for the SED. To do the latter, we compute colour indices from the spectra and then we compare them with those obtained using the observed photometry. If the spectrum is well flux-calibrated, then colour differences should be small.

Photometric colour indices at the epoch of the spectra can be computed through the light-curve fitting procedure presented in Section 4, while to compute a $x_1 - x_2$ colour from a spectrum we use

$$x_1 - x_2 = -2.5 \log \left(\frac{\int d\lambda S_{x_1,\lambda} F_\lambda \lambda}{\int d\lambda S_{x_2,\lambda} F_\lambda \lambda} \right) + \mathrm{ZP}_{x_1-x_2}. \quad \text{(B1)}$$

Here, λ is the wavelength in the observer's frame, F_λ is the observed SED of the source, $S_{x_1,\lambda}$ and $S_{x_2,\lambda}$ are the transmission functions of the photometric band x_1 and x_2, respectively, and $\mathrm{ZP}_{x_1-x_2}$ is the zero-point of the colour scale, which can be computed using a star with good spectrophotometric observations.

We use the Vega SED published by Bohlin & Gilliland (2004)[4] and the magnitudes published by Fukugita et al. (1996): $B_{\mathrm{Vega}} = 0.03$, $V_{\mathrm{Vega}} = 0.03$, and $I_{\mathrm{Vega}} = 0.024$ mag, and by Cohen et al. (1999): $J_{\mathrm{Vega}} = -0.001$, $H_{\mathrm{Vega}} = 0.000$, and $K_{\mathrm{Vega}} = -0.001$ mag. We adopt the transmission functions given in Hamuy et al. (2001). For B–V, V–I, J–H, and H–K we obtained $\mathrm{ZP}_{B-V} = 0.425$, $\mathrm{ZP}_{V-I} = 0.320$, $\mathrm{ZP}_{J-H} = 0.131$, and $\mathrm{ZP}_{H-K} = -0.077$ mag, respectively.

Among the SN II spectra available from different sources, we select those: (1) observed in the photospheric phase, and (2) covered by B- and V-band photometry. To check the flux-calibration in the blue and red part of the optical spectra, we compute $\Delta_{x_1-x_2} \equiv (x_1-x_2)_{\mathrm{phot}} - (x_1-x_2)_{\mathrm{spec}}$ using the B–V and V–I colours, respectively, while for the near-IR spectra we use the J–H and H–K colours, respectively. We also compute the intrinsic B–V colour to represent the shape of the SED. For optical spectra we compute this quantity from dereddened and deredshifted spectra, while for near-IR we compute the intrinsic B–V colour from the photometry (see Section C).

Fig. B1 shows the values of Δ_{B-V} and Δ_{V-I} (top), and Δ_{J-H} and Δ_{H-K} (bottom), along with the intrinsic B–V values for the collected spectra. For the SN II spectra library, we select spectra with $|\Delta_{x_1-x_2}| < 0.1$ mag. Finally, we correct spectra for redshift and for Galactic and host galaxy extinction, assuming a Fitzpatrick (1999) extinction curve with $R_V = 3.1$ for both our Galaxy and hosts.

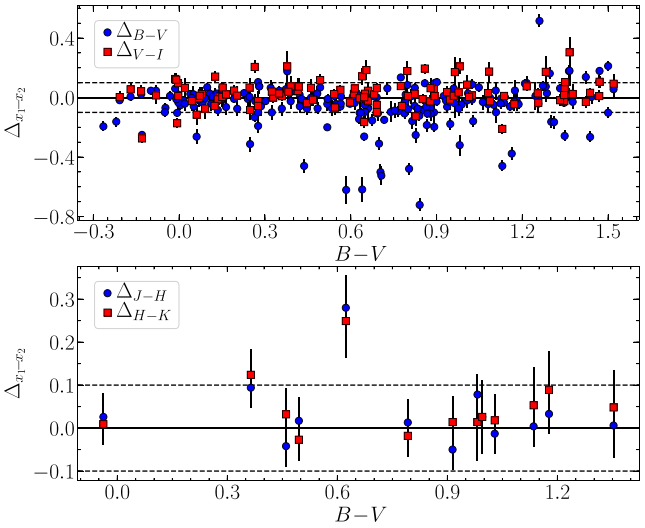

Figure B1. Differences between photometric and spectroscopic colours, along with the intrinsic B–V colour. Dashed lines indicate differences within ± 0.1 mag.

Table F5 summarizes the details of the spectra in the library: SN name (Column 1), Galactic colour excess (Column 2), heliocentric redshift (Columns 3), host galaxy colour excess (Column 4), and references for the data (Column 5).

APPENDIX C: C3 LINEARITY

Assuming that a C3 can be well represented by a polynomial fit, the linearity of a C3 can be demonstrated if there is a high fraction of SNe II showing C3s with straight line as optimal polynomial. Due to the scarcity of K-band photometry, we use only $BVIJH$ photometry for this analysis.

With $BVIJH$ photometry set it is possible to define a total of 10 colour indices and, therefore, 90 colour–colour plots (i.e. discarding one-to-one correlations). Among them, only 36 combinations give us non-superfluous information, which we analyse for host galaxy colour excess estimation.

Before computing intrinsic C3 slopes, photometry must be corrected for Galactic and host galaxy extinction, and for K-correction. Since we need the prior knowledge of the intrinsic B–V, we need to know in advance the value of host galaxy colour excess. For the latter, we apply zero-order correction as prior values. The intrinsic B–V can be computed easily from the relation between the observed and the intrinsic B–V colour, i.e.

$$(B-V)_{\mathrm{obs}} = B-V + (R_B^{\mathrm{G}} - R_V^{\mathrm{G}}) \cdot E_{\mathrm{G}}(B-V) + (K_B^{\mathrm{s}}/z - K_V^{\mathrm{s}}/z) \cdot z + (R_B^{\mathrm{h}} - R_V^{\mathrm{h}}) \cdot E_{\mathrm{h}}(B-V), \quad \text{(C1)}$$

where $(B$–$V)_{\mathrm{obs}}$ is the observed B–V. In Sections 5, 6, and 7 we found that R_V^{G}, K_B^{s}/z, K_V^{s}/z are linear on B–V, while R_B^{G}, R_B^{h}, and R_V^{h} are quadratic on B–V. Therefore, solving a quadratic equation, we can obtain B–V in terms of $(B$–$V)_{\mathrm{obs}}$, $E_{\mathrm{G}}(B$–$V)$, z, $E_{\mathrm{h}}(B$–$V)$, and the fit parameters of R_B^{G}, R_V^{G}, K_B^{s}/z, K_V^{s}/z, R_B^{h}, and R_V^{h}.

For each SN and for each colour combination, we adjust a polynomial fit. The optimum degree is determined using the AIC/BIC and the principle of parsimony.

[4] ftp://ftp.stsci.edu/cdbs/current_calspec/alpha_lyr_stis_008.fits

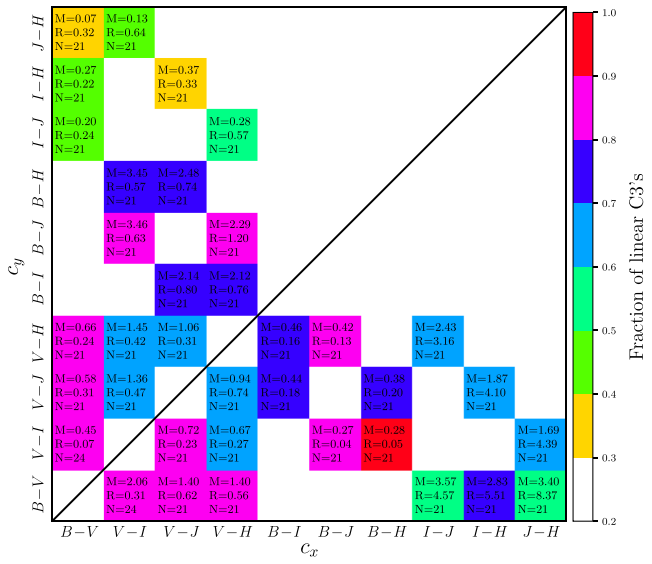

Figure C1. Fraction of linear C3s (colourbar) for different colour combinations, along with the median (M) and the rms (R) of the C3 slopes measured from N SNe in our set. Empty spaces correspond to superfluous colour combinations.

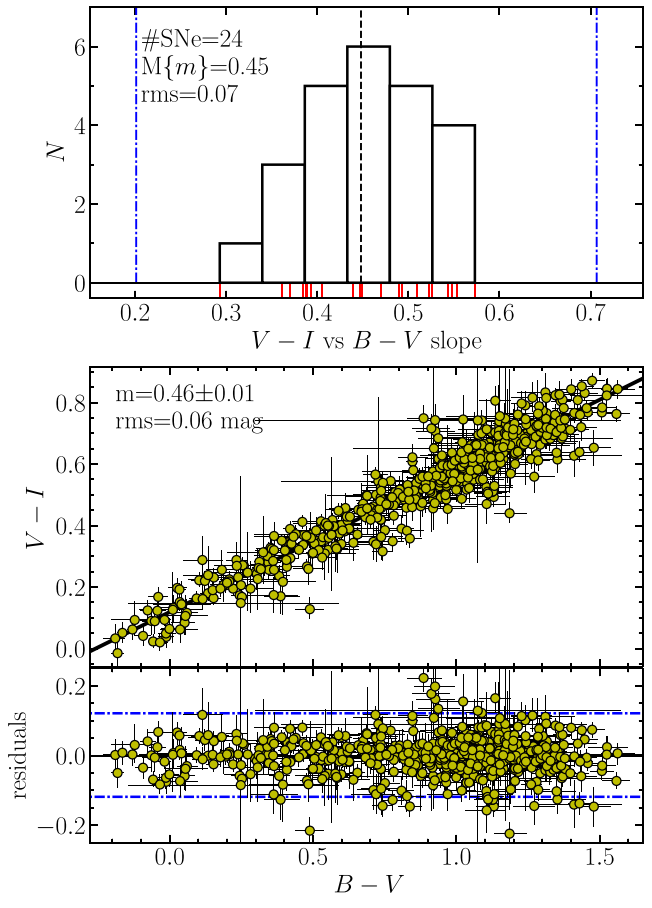

Figure C2. Top: *V–I* versus *B–V* C3 slopes distribution for the SNe in our set. Red ticks mark the specific slope values, and black dashed line marks the median of the slopes. Bottom: *V–I* versus *B–V* diagram showing the 24 SNe II dereddened using host galaxy colour excesses from the C3 method, along with residuals. In both panels, blue dash-dotted lines are the inner fences.

Fig. C1 shows the fraction of SNe that are well represented by a straight line. In 20 of the 36 colour combinations, the number of SNe displaying a linear C3 is over 70 per cent.

Assuming the C3 linearity for different combinations, we compute slopes of all SNe in our set. For each colour combination we compute the median and rms of the C3 slopes. Fig. C2 shows this process for the *V–I* versus *B–V* C3s.

APPENDIX D: SNID EXPLOSION EPOCHS

To estimates phases of SNe II with SNID, we follow similar procedures done by Blondin & Tonry (2007), Silverman et al. (2012), and Gutiérrez et al. (2017).

Among the spectra available from different sources, we select spectra: (1) of SNe II with explosion epoch constrained within 10 d through photometric information, where for these SNe we assume the mid-point between the last non-detection and the first detection as the explosion epoch ($t_{0,\,\ln}$), (2) spanning a rest-frame wavelength range from 4100 to 7000 Å with an S/N $\gtrsim 10\,\text{Å}^{-1}$, and (3) within 40 d since the explosion epoch. We do not include spectra at >40 d since explosion because in literature it is less abundant than spectra at earlier epochs (see e.g. Fig. 5 in Gutiérrez et al. 2017) which could bias the age determination towards earlier epochs, and also because at late time the spectral evolution is slower than at early phases, which makes more difficult to accurately determine ages with SNID (Blondin & Tonry 2007). If for a given epoch an SN has several spectra within 1 d, then we keep that with higher S/N. With the aforementioned constraints, we generate an SNID template library with 242 spectra of 56 SNe II, where each spectrum is corrected by heliocentric redshift. Details of this SN II templates library are summarized in Table F6.

Fig. D1 shows the phase distribution of the templates. The library has, on average, 6 spectra per day, while almost all the variation is within ±2 rms around the mean.

To create the template library, we run the `logwave` routine (which is part of the SNID program) with the options `w0=3000 w1=8400 nw = 1024`. This generates SNID spectral templates with a bin in the logarithmic wavelength space of ln(8400/3000)/1024≈0.001, equivalent to 300 km s^{-1}.

Once the template library is created, the next step is to test how good are the phases since explosion computed with SNID and our

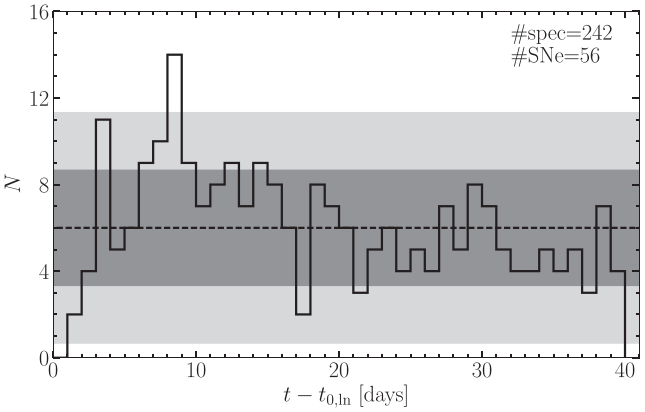

Figure D1. Phase distribution of the templates in our SNID SN II library. The dashed line indicates the average of spectra per bin, while dark grey and light grey regions contain values within ±1 and ±2 rms around the mean, respectively.

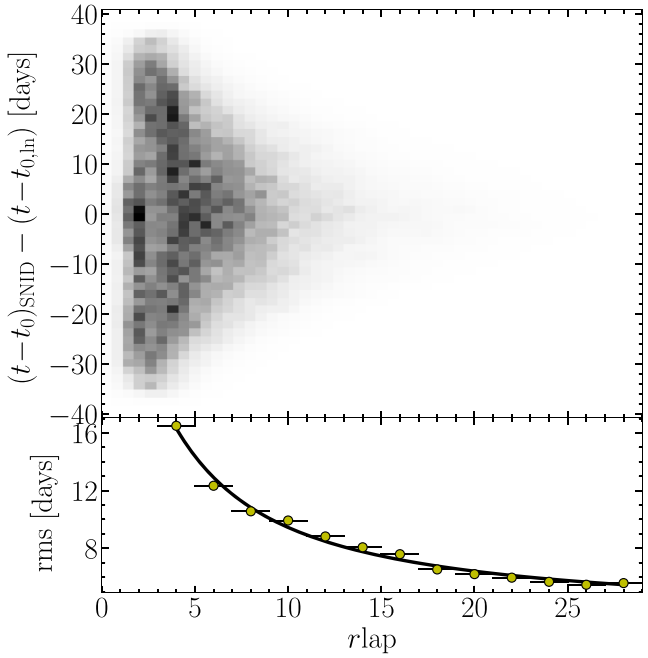

Figure D2. 2D histogram of differences between phases since explosion estimated from last non-detection ($t - t_{0,\,\rm ln}$) and from SNID $(t - t_0)_{\rm SNID}$ versus the *r*lap parameter (top), and the rms of phase differences versus *r*lap (bottom).

new library. To do this, we run SNID with each library spectrum as input, using the `avoid` option to avoid templates of the same SN. We record all phases and *r*lap values (which indicate the correlation strength) of the templates found to be similar to the input spectrum and with a redshift within ±0.01. The top panel of Fig. D2 shows the 2D histogram of differences between phases since explosion estimated from last non-detection and from SNID, versus *r*lap. To correlate *r*lap with an rms error in phase, we compute the rms of phase differences in bins of width 2 *r*lap, which is shown at bottom of Fig. D2. To convert *r*lap to an rms error, we fit a 1/*r*lap polynomial of order 2 (determined by the AIC/BIC), given by

$$\rm rms = (3.0 + 72.0/\mathit{r}lap - 75.0/\mathit{r}lap^2)\ d. \quad (D1)$$

In general, only one spectrum (e.g. the earliest) is used to estimate explosion epochs with SNID (e.g. Anderson et al. 2014b; Gutiérrez et al. 2017). We expect, however, that including all available spectra of an SN in the analysis will result in a best estimation of the explosion epoch. To explore this possibility, we select all SNe in our library with five or more spectra and perform the following procedure:

(1) For each SN we randomly choose one spectrum, computing the explosion epoch ($t_{0,\,\rm SNID}$) and $t_{0,\,\rm SNID} - t_{0,\,\rm ln}$.
(2) We compute the median (i.e. the offset) and the rms of the $t_{0,\,\rm SNID} - t_{0,\,\rm ln}$ distribution.
(3) We repeat steps 1 and 2 10^2 times, recording the median of the offsets and the rms values.
(4) We repeat steps 1–3, but now randomly choosing two and then three spectra per SN as input.

Table D1 shows the result of the aforementioned process, i.e. the offset and the rms as a function of the number of input spectra. Using only one spectrum we obtain a typical rms of 5.0 d, which is similar than the rms of 5.2 d reported by Gutiérrez et al. (2017).

Table D1. Result of SNID simulations.

# of input spectra	Md($t_{0,\,\rm SNID} - t_{0,\rm ln}$) (d)	rms($t_{0,\,\rm SNID} - t_{0,\rm ln}$) (d)
1	$-0.6^{+1.0}_{-0.6}$	$5.0^{+0.9}_{-0.6}$
2	$-0.7^{+0.9}_{-0.7}$	$4.1^{+0.9}_{-0.4}$
3	$-0.6^{+0.6}_{-0.9}$	$4.1^{+0.2}_{-0.4}$

Table D2. Observed quantities of SN 1980K and SN 2002hh.

SN	Δt (d)	J (mag)	$v_{\rm ph}$ (km s^{-1})	$E_{\rm h}(B–V)$ (mag)	References[b]
1980K	$54.4^{+7.7}_{-7.2}$	$11.29^{+0.06}_{-0.05}$	4013^{+165}_{-143}	0.0	1, 2, 3, 4, 5
2002hh	$44.5^{+2.0}_{-2.0}$	$12.30^{+0.04}_{-0.04}$	4714^{+53}_{-56}	2.74 ± 0.11[a]	6, 7, 8, 9

[a]The colour excess was computed adopting the Cardelli et al. (1989) extinction curve and $R_V = 1.9$ (Pozzo et al. 2006). For that extinction curve, we obtained $R^{\rm h}_J = 0.402$.
[b](1) IAUC 3532; (2) Thompson (1982); (3) Dwek et al. (1983); (4) Schmidt et al. (1992); (5) WISeREP; (6) IAUC 8005; (7) IAUC 8024; (8) Pozzo et al. (2006); and (9) Faran et al. (2014a).

We see that using more than one spectrum the rms is reduced down to 4.1 d. The median of the offsets is around −0.6 d, independent of the number of input spectra in the analysis. This offset means that explosion epochs computed with SNID are 0.6 d earlier than those estimated with the non-detection. Hereafter, for the explosion epochs derived with SNID we assume an intrinsic error of 5.0 d when only one spectrum is used, or 4.1 d whether more spectra are available.

APPENDIX E: THE DISTANCE TO NGC 6946

The distance to NGC 6946, host of SN 2004et, was measured with the TRGB method by Tikhonov (2014, hereafter T14), Murphy et al. (2018, hereafter M18), and Anand et al. (2018, hereafter A18), and correspond to $\mu = 29.39 \pm 0.14$ mag in the Jang & Lee (2017a) calibration. The PMM *J*-band distance for SN 2004et obtained in this work ($\mu_J = 28.83 \pm 0.12$ mag) is in conflict with the TRGB estimation. To investigate the reason for this discrepancy, we compute distances to other two SNe II that exploded in NGC 6946: SN 1980K and SN 2002hh. These SNe have near-IR photometry, but we did not include them into the analysis because they do not have photometry in the five bands we use (i.e. *BVIJH*).

Using data given in Table D2 , we obtain $\mu_J = 28.73 \pm 0.18$ and 28.77 ± 0.11 mag for SN 1980K and SN 2002hh, respectively, which are consistent with the distance computed with SN 2004et. There is then a tension of at least ∼4 rms between the PMM and the TRGB distance. This discrepancy could be due to: (1) all three SNe II are intrinsically brighter at least 0.56 mag than the SNe II we use for the calibration, or (2) there are issues with the TRGB distances reported by T14, M18, and A18. We noted that the latter two independent studies used almost the same data but obtained significantly different values of the TRGB F814W magnitude ($\rm F814W_{TRGB}$): 26.00 ± 0.04 mag in M18 and 25.84 ± 0.11 mag in A18. T14 used another set of image data, which is closer to the centre of the galaxy than those used in M18 and A18, and obtained a lower $\rm F814W_{TRGB}$ value (25.79 ± 0.05 mag). At this moment, the origin of this large discrepancy is unclear. Taking this into account, we safely remove SN 2004et from the calibration and the final sample.

APPENDIX F: TABLES

Table F1. Akaike and Bayesian weights, and evidence ratios for $R_x^{\rm G}$, $K_x^{\rm s}/z$, $R_x^{\rm h}$, and $f_{x,\,\Delta t}$. The full table is available online.

	$R_B^{\rm G}$				$R_V^{\rm G}$				$R_I^{\rm G}$			
i^a	w_i	$\rm P_i$	$\frac{w_6}{w_i}$	$\frac{\rm P_2}{\rm P_i}$	w_i	$\rm P_i$	$\frac{w_2}{w_i}$	$\frac{\rm P_2}{\rm P_i}$	w_i	$\rm P_i$	$\frac{w_4}{w_i}$	$\frac{\rm P_1}{\rm P_i}$
0	0.00	0.00	–	–	0.00	0.00	–	–	0.00	0.00	–	–
1	0.00	0.00	–	–	0.05	0.34	7.4	1.8	0.14	0.76	2.3	1.0
2	0.02	0.50	19.5	1.0	0.37	0.60	1.0	1.0	0.05	0.09	6.4	8.4
3	0.03	0.21	13.0	2.4	0.16	0.06	2.3	10.0	0.02	0.01	16.0	76.0
4	0.10	0.16	3.9	3.1	0.06	0.00	6.2	–	0.32	0.09	1.0	8.4
5	0.23	0.09	1.7	5.6	0.04	0.00	9.2	–	0.30	0.04	1.1	19.0
6	0.39	0.04	1.0	12.5	0.12	0.00	3.1	–	0.12	0.01	2.7	76.0
7	0.14	0.00	2.8	–	0.06	0.00	6.2	–	0.03	0.00	10.7	–
8	0.09	0.00	4.3	–	0.15	0.00	2.5	–	0.02	0.00	16.0	–
	$R_J^{\rm G}$				$R_H^{\rm G}$				$R_K^{\rm G}$			
i^a	w_i	$\rm P_i$	$\frac{w_0}{w_i}$	$\frac{\rm P_3}{\rm P_i}$	w_i	$\rm P_i$	$\frac{w_0}{w_i}$	$\frac{\rm P_3}{\rm P_i}$	w_i	$\rm P_i$	$\frac{w_1}{w_i}$	$\frac{\rm P_6}{\rm P_i}$
0	0.80	0.18	1.0	2.8	0.81	0.20	1.0	2.3	0.06	0.00	13.2	–
1	0.13	0.05	6.2	10.0	0.13	0.06	6.2	7.7	0.79	0.09	1.0	2.9
2	0.01	0.01	80.0	50.0	0.01	0.02	81.0	23.0	0.12	0.06	6.6	4.3
3	0.06	0.50	13.3	1.0	0.05	0.46	16.2	1.0	0.03	0.16	26.3	1.6
4	0.00	0.17	–	2.9	0.00	0.14	–	3.3	0.00	0.08	–	3.2
5	0.00	0.06	–	8.3	0.00	0.08	–	5.8	0.00	0.20	–	1.3
6	0.00	0.02	–	25.0	0.00	0.02	–	23.0	0.00	0.26	–	1.0
7	0.00	0.01	–	50.0	0.00	0.02	–	23.0	0.00	0.15	–	1.7

[a]Polynomial order.

Table F2. Fits parameters for $R_x^{\rm G}$, $K_x^{\rm s}/z$, and $R_x^{\rm h}$.

x	$c_{0,\,x}$	$c_{1,\,x}$	$c_{2,\,x}$	rms	p(RM)
		$R_x^{\rm G} = c_{0,x} + c_{1,x}(B-V) + c_{2,x}(B-V)^2$†			
B	$4.074^{+0.003}_{-0.003}$	$-0.107^{+0.014}_{-0.012}$	$-0.046^{+0.010}_{-0.011}$	0.009	0.42
V	$3.089^{+0.002}_{-0.002}$	$-0.048^{+0.003}_{-0.002}$	–	0.006	0.32
I	$1.722^{+0.002}_{-0.002}$	$-0.004^{+0.002}_{-0.002}$	–	0.003	0.86
J	$0.8135^{+0.0008}_{-0.0008}$	–	–	0.0012	0.67
H	$0.5184^{+0.0003}_{-0.0003}$	–	–	0.0004	0.43
K	$0.3484^{+0.0001}_{-0.0001}$	–	–	0.0001	0.46
		$K_x^{\rm s}/z = c_{0,x} + c_{1,x}(B-V)$†,⋄			
B	$0.51^{+0.06}_{-0.06}$	$6.23^{+0.09}_{-0.09}$	–	0.41	0.23
V	$-0.51^{+0.05}_{-0.05}$	$2.87^{+0.07}_{-0.07}$	–	0.35	0.13
I	$-0.40^{+0.11}_{-0.11}$	$1.14^{+0.17}_{-0.17}$	–	0.46	0.53
J	$-0.77^{+0.09}_{-0.09}$	–	–	0.21	0.63
H	$-0.82^{+0.05}_{-0.05}$	–	–	0.14	0.58
K	$-1.40^{+0.05}_{-0.05}$	–	–	0.15	0.61
		$R_x^{\rm h} = c_{0,x} + c_{1,x}(B-V) + c_{2,x}(B-V)^2$†			
B	$4.085^{+0.002}_{-0.003}$	$-0.097^{+0.011}_{-0.010}$	$-0.049^{+0.008}_{-0.009}$	0.008	0.97
V	$3.092^{+0.002}_{-0.002}$	$-0.034^{+0.007}_{-0.007}$	$-0.009^{+0.006}_{-0.005}$	0.006	0.26
I	$1.724^{+0.002}_{-0.002}$	$-0.005^{+0.002}_{-0.002}$	–	0.003	0.95
J	$0.8140^{+0.0008}_{-0.0009}$	–	–	0.0012	0.60
H	$0.5187^{+0.0002}_{-0.0003}$	–	–	0.0004	0.36
K	$0.3485^{+0.0001}_{-0.0001}$	–	–	0.0001	0.58

Note: Fits are valid for $-0.2 < B–V < 1.5$ and $-0.05 < B–V < 1.35$ for *BVI* and *JHK*, respectively (†), and $z < 0.032$ (⋄). Errors are the 99 per cent CI.

Table F3. SN II parameters. The full table is available online.

SN	$E_h(B–V)$ {$B–V$, $V–I$}	$E_h(B–V)$ O10	Discovery (JD)	t^a_{ln} (d)	t^a_{fd} (d)	$t^a_{0,SNID}$ (d)	$t^a_{0,final}$ (d)	References[d]
1999em	$0.035^{+0.105}_{-0.105}(0.082)$	0.106(0.052)	2451480.94	−8.99	−1.43	−6.37(4.16)	$-5.57^{+2.96}_{-2.63}$	IAUC 7294, E03
2002gd	$0.154^{+0.111}_{-0.106}(0.084)$	–	2452553.37	−4.09[b]	−2.84[b]	0.73(4.48)	$-3.42^{+0.46}_{-0.53}$	IAUC 7986, IAUC 7990
2002gw	$0.202^{+0.106}_{-0.108}(0.084)$	0.132(0.061)	2452560.77	−31.218	−1.637	−4.29(4.28)	$-5.74^{+3.22}_{-4.73}$	IAUC 7995, IAUC 7996

Notes: Column 1: SN names. Column 2: host galaxy colour excesses estimated with the $V–I$ versus $B–V$ C3, where errors correspond to the 80 per cent CI, and the rms in parenthesis. Column 3: host galaxy colour excesses from Olivares E. et al. (2010) recalibrated by R14, with rms in parenthesis. Column 4: discovery epochs. Columns 5 and 6: last non-detection and first detection epochs, respectively. Columns 7 and 8: explosion epochs estimated with SNID and our SN II template library, without any prior (rms error in parenthesis) and with photometric priors, respectively. Column 9: references for discovery, last non-detection, and first detection epochs.

[a]Epochs with respect to the discovery epoch.

[b]Value obtained through polynomial fits to pre-maximum *VRI* photometry.

[c]Optical spectra not published.

[d]E03: Elmhamdi et al. (2003); P09: Pastorello et al. (2009); R11: Roy et al. (2011); F11: Fraser et al. (2011); CF: C. Feliciano report on the *Bright Supernova* website (http://www.rochesterastronomy.org/snimages/).

Table F4. CMB redshifts and PMM distance moduli. The full table is available online.

Galaxy	cz_{CMB} (km s^{-1})	SN	μ_B	μ_V	μ_I	μ_J	μ_H
NGC 6946	−141(382)	2004et	$28.40^{+0.60}_{-0.60}(0.47)$	$28.57^{+0.45}_{-0.45}(0.35)$	$28.67^{+0.27}_{-0.27}(0.21)$	$28.83^{+0.15}_{-0.15}(0.12)$	$28.75^{+0.11}_{-0.11}(0.09)$
M74	359(383)	2013ej	$30.21^{+0.56}_{-0.56}(0.44)$	$30.08^{+0.42}_{-0.42}(0.33)$	$30.02^{+0.25}_{-0.25}(0.20)$	$29.94^{+0.14}_{-0.14}(0.11)$	$29.94^{+0.11}_{-0.11}(0.09)$
M51a	636(382)	2005cs	$29.62^{+0.51}_{-0.51}(0.40)$	$29.57^{+0.39}_{-0.39}(0.30)$	$29.54^{+0.24}_{-0.24}(0.19)$	$29.61^{+0.14}_{-0.14}(0.11)$	$29.61^{+0.11}_{-0.11}(0.09)$

Note: We adopt $R_V = 3.1$ for our Galaxy and hosts. Errors are the 80 per cent CI and rms (in parenthesis), and include the TRGB zero-point systematic error.

Table F5. SNII spectra library. The full table is available online.

SN	$E_G(B–V)^a$ (mag)	cz_{helio} (km s^{-1})	$E_h(B–V)^b$ (mag)	References[d]	SN	$E_G(B–V)^a$ (mag)	cz_{helio} (km s^{-1})	$E_h(B–V)^b$ (mag)	References[d]
1990E	0.022	1362	0.616	1	2003Z	0.033	1289	0.065	5, 7
1992ba	0.050	1135	0.049	2	2003bl	0.023	4295	0.103	2
1996W	0.036	1617	0.252	3	2003bn	0.056	3897	0.019	2

[a]Values from Schlafly & Finkbeiner (2011).

[b]Values computed in this work.

[c]SN with useful near-IR spectra.

[d](1) Schmidt et al. (1993); (2) Gutiérrez et al. (2017); (3) Inserra et al. (2013); (4) Pastorello et al. (2004); (5) Faran et al. (2014a); (6) Faran et al. (2014b); (7) Spiro et al. (2014); (8) Pastorello et al. (2006); (9) Pastorello et al. (2009); (10) Takáts et al. (2014); (11) Takáts et al. (2015); (12) Dall'Ora et al. (2014); (13) Barbarino et al. (2015); (14) Valenti et al. (2014); (15) Dhungana et al. (2016); (16) Yuan et al. (2016); and (17) Terreran et al. (2016).

Table F6. SNID templates. The full table is available online.

SN	t_d (d)	$t_{ln} - t_d$ (d)	$t_{fd} - t_d$ (d)	$t - t_{0,ln}$ (d)	References[c]
1986L	2446711.1	−5.6	0.0	6,7,[27:33]	IAUC 4260, 1
1988A	2447179.299	−3.099	−1.968	13	IAUC 4533, IAUC 4540, 1
1990E	2447937.62	−5.12	0.0	9,19	IAUC 4965, 2

Notes: Column 1: SN names. Column 2: discovery epochs. Column 3 and 4: last non-detection and first detection epochs, respectively, with respect to the discovery epoch. Column 5: spectra phase values with respect to the explosion epoch, which we assume as the mid-point between the last non-detection and the first detection. Adjacent ages are listed in brackets. Column 6: references for data.

[a]Explosion time constraint obtained through polynomial fit to pre-maximum *VRI* photometry.

[b]C. Feliciano report on the *Bright Supernova* website (http://www.rochesterastronomy.org/snimages/)

[c](1) Gutiérrez et al. (2017); (2) Schmidt et al. (1993); (3) Pastorello et al. (2004); (4) Elmhamdi et al. (2003); (5) Faran et al. (2014a); (6) Shivvers et al. (2017); (7) Faran et al. (2014b); (8) Hicken et al. (2017); (9) Harutyunyan et al. (2008); (10) Spiro et al. (2014); (11) Sahu et al. (2006); (12) Gal-Yam et al. (2008); (13) Pastorello et al. (2009); (14) Pastorello et al. (2006); (15) Quimby et al. (2007); (16) Sako et al. (2018); (17) Inserra et al. (2013); (18) Gal-Yam et al. (2011); (19) Dall'Ora et al. (2014); (20) Tomasella et al. (2018); (21) Zhang et al. (2014); (22) Valenti et al. (2015); (23) Valenti et al. (2014); (24) Childress et al. (2016); (25) Dhungana et al. (2016); (26) Yuan et al. (2016); (27) Yaron et al. (2017); (28) Terreran et al. (2016); and (29) Valenti et al. (2016).

This paper has been typeset from a TEX/LATEX file prepared by the author.